Optical spatial dispersion via Wannier interpolation

Andrea Urru,[1,*] Ivo Souza,[2,3,*] Óscar Pozo Ocaña,[2] Stepan S. Tsirkin,[2,3,4] and David Vanderbilt[1]

[1]*Department of Physics & Astronomy, Rutgers University, Piscataway, New Jersey 08854, USA*

[2]*Centro de Física de Materiales, Universidad del País Vasco, 20018 San Sebastián, Spain*

[3]*Ikerbasque Foundation, 48013 Bilbao, Spain*

[4]*Chair of Computational Condensed Matter Physics, Institute of Physics, École Polytechnique Fédérale de Lausanne (EPFL), CH-1015 Lausanne, Switzerland*

(Received 12 April 2025; accepted 27 June 2025; published 14 July 2025)

We present a numerical implementation, based on Wannier interpolation, of a Kubo-Greenwood formalism for computing the spatially dispersive optical conductivity in crystals at first order in the wave vector of light. This approach is more efficient than direct *ab initio* methods because, with less computational cost, it allows for a much finer sampling of reciprocal space, resulting in better-resolved spectra. Moreover, Wannier interpolation avoids errors arising from truncation of the sums over conduction bands when evaluating the spatially dispersive optical matrix elements. We validate our method by computing the optical activity spectrum of selected crystals, both polar (GaN) and chiral (trigonal Te, trigonal Se, and α-quartz), and comparing it with existing literature.

DOI: 10.1103/56cw-5h19

I. INTRODUCTION

When the wavelength of light is long compared to typical atomic dimensions and bond lengths, the optical response of a medium can be treated as local in space and, thus, does not depend on the wave vector **q** of incident radiation. Beyond this approximation, **q**-dependent contributions to the optical response, corresponding to spatially dispersive—i.e., nonlocal—effects, must be taken into account [1]. Despite usually being small corrections, spatial-dispersion terms describe phenomena that are not captured by the **q**-independent optical response. Among them we mention natural optical activity (optical activity henceforth), which stems from the first-order spatial dispersion of the optical conductivity and shows up in acentric systems. A well-known manifestation of optical activity is optical rotation, i.e., the rotation of the plane of polarization of incident linearly polarized light as it travels through a chiral medium [1–5]. Besides optical activity, optical spatial dispersion phenomena also include magneto-optical effects such as gyrotropic birefringence [5–8] and nonreciprocal directional dichroism [9], which occur in acentric magnetic crystals (e.g., the antiferromagnet Cr_2O_3).

Due to the fundamental interest in chiral molecules and their relevance for industry, historically optical activity has been studied more extensively in molecules than in solids. Starting a few decades ago, several *ab initio* approaches for computing optical activity in molecules have been developed [10–16], based on earlier molecular quantum theories. Until a few years ago, not as many attempts to formulate an equivalent theory for periodic solids had been made [17–19]. More recently, increased interest in chiral crystals has brought renewed attention to optical activity and related phenomena. This has fostered the development of first-principles theories of spatial dispersion in bulk periodic systems [20–22].

Currently, the available *ab initio* implementations of optical spatial dispersion in solids follow one of two distinct approaches: Kubo-Greenwood linear-response theory, or density-functional perturbation theory (DFPT). Methods based on the Kubo formulation [20,21] have a practical advantage over the DFPT-based approaches [22] because of their ease of implementation. Indeed, while Kubo linear response theory can be implemented as a postprocessing step after a ground-state self-consistent first-principles calculation, DFPT requires the self-consistent solution of a more involved Sternheimer linear system, besides the ground-state calculation. Moreover, current DFPT implementations typically access only the zero-frequency limit of optical activity, while the Kubo approach naturally accounts for the frequency dependence of the response. On the other hand, the DFPT formulation carefully accounts for the induced variation of the self-consistent potentials (Hartree and exchange-correlation), which can be large in some cases [22,23]. Such local-field effects are neglected in current implementations of the Kubo formalism—including the present one—which treat the self-consistent potentials as frozen quantities, neglecting their response to the electromagnetic perturbation.

A Kubo approach for computing the spatially dispersive optical conductivity has recently been proposed in two different ways in Refs. [20] and [21], building on an earlier work [19]. Both formulations take the molecular multipole theory of electromagnetism [2,5] as a basis, and recast the multipolar terms in a way that is suitable for crystals as well. One drawback of the Kubo approach is connected with the need to use a sufficiently dense **k** mesh to resolve the features of interest in optical spectra. This requires a self-consistent solution at every point on this dense mesh, which is computationally expensive. A second drawback is that in practice

[*]These authors contributed equally to this work.

the sum over states in the formulation of Ref. [20] has to be truncated.

Here, we elaborate on the formulation of Ref. [21] and present an *ab initio* implementation of the Kubo formalism using Wannier interpolation [24–26]. This technique allows for a very fine sampling of reciprocal space with a much lower computational cost than a direct *ab initio* calculation. Furthermore, it avoids sums over intermediate states when evaluating the optical matrix elements at first order in $\mathbf{q}$, and is therefore expected to be less affected by band truncation errors. We test our implementation by computing the optical activity of both polar (GaN) and chiral (Te, Se, and α-SiO_2) crystals, and by comparing our results with existing literature, both theoretical [20,22] and experimental [27,28].

The remainder of the paper is organized in the following way. In Secs. II-IV we present the underlying theoretical formalism and the relevant details related to the implementation. We start in Sec. II by recapitulating the general properties of the spatially dispersive optical response and its expression in the Kubo formalism. In Sec. III we discuss a sum-over-states approach for evaluating the Kubo formula for the conductivity. Although this is not the method implemented in this work, we find it instructive to discuss it and to compare with our approach, which we present in the following section. Specifically, in Sec. IV A we introduce the Wannier interpolation scheme, and in Sec. IV B we show how to use it to evaluate the spatially dispersive optical conductivity. In Sec. V we present our numerical results and validate our implementation by comparing with previous literature. Finally, Sec. VI contains a summary and conclusions. We conclude the paper with four Appendices, containing analytical derivations and some numerical tests.

II. OPTICAL SPATIAL DISPERSION

A. Phenomenology

The optical response of a medium to a monochromatic electromagnetic wave is described by the dielectric function ϵ, which relates the induction field $\mathbf{D}$ to the incident wave's electric field $\mathbf{E}$. In the reciprocal variables ω and $\mathbf{q}$ (frequency and wave vector), this relationship reads [1]

$$D_\alpha(\omega, \mathbf{q}) = \epsilon_{\alpha\beta}(\omega, \mathbf{q}) E_\beta(\omega, \mathbf{q}), \tag{1}$$

where summation over repeated indices is implied, a convention that we adopt henceforth, and α and β are Cartesian indices. In general, the response of a periodic medium to a perturbation with wave vector $\mathbf{q}$ has contributions from all $\mathbf{q}+\mathbf{G}$ wave vectors, with the $\mathbf{G} \neq \mathbf{0}$ components resulting from variations of the $\mathbf{D}$ field at spatial scales of the order of the bond lengths. This fact underlies the presence of local-field corrections, which are not included in this work, as mentioned in the Introduction. The dielectric function can be Taylor-expanded as [1]

$$\epsilon_{\alpha\beta}(\omega, \mathbf{q}) = \epsilon_{\alpha\beta}(\omega, \mathbf{0}) + i\eta_{\alpha\beta\gamma}(\omega) q_\gamma + \dots. \tag{2}$$

Here, $\epsilon_{\alpha\beta}(\omega, \mathbf{0})$ is the dielectric function in the infinite-wavelength limit, and $\eta_{\alpha\beta\gamma}(\omega)$ describes spatial-dispersion effects at first order in $\mathbf{q}$.

The $\eta_{\alpha\beta\gamma}$ tensor is odd under spatial inversion $\mathcal{P}$, and thus vanishes identically in centrosymmetric crystals. To analyze its behavior under time-reversal $\mathcal{T}$, we split $\eta_{\alpha\beta\gamma}$ into symmetric (S) and antisymmetric (AS) parts under permutation of α and β,

$$\eta_{\alpha\beta\gamma}(\omega) = \eta^{\mathrm{S}}_{\alpha\beta\gamma}(\omega) + \eta^{\mathrm{AS}}_{\alpha\beta\gamma}(\omega). \tag{3}$$

As a consequence of Onsager's reciprocity relation, $\eta^{\mathrm{AS}}_{\alpha\beta\gamma}$ is $\mathcal{T}$-even while $\eta^{\mathrm{S}}_{\alpha\beta\gamma}$ is $\mathcal{T}$-odd. $\eta^{\mathrm{AS}}_{\alpha\beta\gamma}$ describes *natural optical activity* (optical activity henceforth), which requires broken $\mathcal{P}$ but not broken $\mathcal{T}$. $\eta^{\mathrm{S}}_{\alpha\beta\gamma}$ accounts for spatially dispersive *magneto-optical effects* in materials where both $\mathcal{P}$ and $\mathcal{T}$ symmetries are broken (but the combined $\mathcal{PT}$ may be present). The $\mathcal{T}$-odd effects are *nonreciprocal* in that one sees distinct behaviors for forward vs backward propagation of light. The tensors $\eta^{\mathrm{AS}}_{\alpha\beta\gamma}$ and $\eta^{\mathrm{S}}_{\alpha\beta\gamma}$ can be further decomposed as

$$\eta^{\mathrm{S}}_{\alpha\beta\gamma}(\omega) = \mathrm{Re}\,\eta^{\mathrm{H}}_{\alpha\beta\gamma}(\omega) + i\mathrm{Im}\,\eta^{\mathrm{AH}}_{\alpha\beta\gamma}(\omega), \tag{4a}$$

$$\eta^{\mathrm{AS}}_{\alpha\beta\gamma}(\omega) = \mathrm{Re}\,\eta^{\mathrm{AH}}_{\alpha\beta\gamma}(\omega) + i\mathrm{Im}\,\eta^{\mathrm{H}}_{\alpha\beta\gamma}(\omega) \tag{4b}$$

into Hermitian (H) and anti-Hermitian (AH) parts related to absorptive and reactive phenomena, respectively.

As our main focus is on optical activity, we analyze $\eta^{\mathrm{AS}}_{\alpha\beta\gamma}$ in more detail. Being a rank-3 tensor antisymmetric in two indices, it has nine independent components that can be repackaged as a rank-2 *gyration tensor* G by contracting with the Levi-Civita symbol $\varepsilon_{\alpha\gamma\delta}$. Following Refs. [22,29], we define the complex gyration tensor as

$$G_{\alpha\beta}(\omega) = \tfrac{1}{2}\,\varepsilon_{\alpha\gamma\delta}\,\eta^{\mathrm{AS}}_{\gamma\delta\beta}(\omega). \tag{5}$$

With this definition, G has units of length and tends to a real-valued constant in the $\omega \to 0$ limit [22,30].

It is useful to decompose G into a trace piece, a traceless symmetric part, and an antisymmetric part [29]. The first two form the symmetric part of G, whose real and imaginary components account for optical rotation and circular dichroism, respectively, of light propagating along an optic axis.

Optical rotation—the rotation of the plane of polarization of linearly polarized incident light—results from a different speed of propagation of left and right circular components. It is quantified by the optical rotatory power, defined as the angle of rotation of the plane of polarization of light per unit distance traveled inside the material. Circular dichroism is the absorptive counterpart of optical rotation, and corresponds to different absorption coefficients for left and right circular components. As a result, a linearly polarized incident wave develops an elliptical character as one of its circular components decays more quickly than the other. For light not propagating along an optic axis, linear birefringence typically dominates, but the modes of propagation acquire some elliptical character. The rotatory power ρ and ellipticity θ are obtained from the real and imaginary parts of G as [1]

$$\rho(\omega) + i\theta(\omega) = \frac{\omega^2}{2c^2}\hat{q}_\alpha[\mathrm{Re}\,G_{\alpha\beta}(\omega) + i\mathrm{Im}\,G_{\alpha\beta}(\omega)]\hat{q}_\beta \tag{6}$$

with $\hat{\mathbf{q}}$ the unit vector along the propagation direction $\mathbf{q}$, assumed to be an optic axis, and c the speed of light. As anticipated, ρ and θ only depend on the symmetric part of G. Since $\mathrm{Re}\,G$ becomes constant at low frequencies, the rotatory power decreases as ω^2, that is, the quantity

$$\bar{\rho}(\omega) = \frac{\rho(\omega)}{\omega^2} \tag{7}$$

tends to a constant for $\omega \to 0$.

The antisymmetric part of G can be repackaged as a polar vector with components $G_\alpha = (1/2)\varepsilon_{\alpha\beta\gamma}G_{\beta\gamma}$. This describes a situation in which the electric polarization vector of the beam acquires a small longitudinal component [29]. For example, light entering along x with polarization z can propagate in the medium with a slight elliptical polarization in the x-z plane. By analogy with Eq. (6), one may quantify this "polar optical activity" via a complex vector $\mathbf{d}(\omega)$ with units of inverse length,

$$\mathbf{d}(\omega) = \frac{\omega^2}{2c^2}\mathbf{G}(\omega). \tag{8}$$

Of the 21 acentric crystal classes, 18 allow for a nonzero gyration tensor G. We identify as *optically active* a material belonging to any of these classes, according to a broad definition [29]. The three acentric classes that do not show optical activity are $\bar{6}$, $\bar{6}2m$, and $\bar{4}3m$. Among the 18 optically active crystal classes, three of them ($3m$, $4mm$, and $6mm$) have a purely antisymmetric G tensor. Materials that belong to these polar classes do not display optical rotation or circular dichroism. Nevertheless, we still classify them here as optically active, while noting that some authors adopt a more stringent definition that would exclude materials such as these [31]. The other 15 classes, which do support optical rotation, include 11 where the trace of G is nonzero. These *chiral* or *enantiomorphic* groups are the only ones for which optical rotation is present even in polycrystalline samples. Chiral materials can exist in two different forms, called enantiomorphs, related to each other by a mirror reflection. The two enantiomorphs show opposite ("dextrogyre" and "levogyre") optical rotation. The remaining four classes ($\bar{4}$, $\bar{4}2m$, $mm2$, and m) have a traceless G tensor. They still show signs of optical rotation and circular dichroism [4], but these effects are mixed with linear birefringence, so that the solutions of the wave equation are elliptically polarized in general.

B. Microscopic theory

In the Kubo linear-response formalism, one calculates the optical conductivity tensor σ relating the induced current density $\mathbf{j}$ to the optical electric field $\mathbf{E}$,

$$j_\alpha(\omega, \mathbf{q}) = \sigma_{\alpha\beta}(\omega, \mathbf{q})E_\beta(\omega, \mathbf{q}). \tag{9}$$

The dielectric function and the optical conductivity are related in CGS units by

$$\epsilon_{\alpha\beta}(\omega, \mathbf{q}) = \delta_{\alpha\beta} + \frac{4\pi i}{\omega}\sigma_{\alpha\beta}(\omega, \mathbf{q}). \tag{10}$$

Expanding the latter in powers of $\mathbf{q}$ as

$$\sigma_{\alpha\beta}(\omega, \mathbf{q}) = \sigma_{\alpha\beta}(\omega, \mathbf{0}) + \sigma_{\alpha\beta\gamma}(\omega)q_\gamma + \dots \tag{11}$$

and comparing with the expansion (2) of the former yields

$$\eta_{\alpha\beta\gamma}(\omega) = \frac{4\pi}{\omega}\sigma_{\alpha\beta\gamma}(\omega), \tag{12}$$

which combined with Eq. (5) expresses the gyration tensor in terms of the spatially dispersive conductivity.

The spatially dispersive optical conductivity evaluated from Kubo linear response is given by the following expression, equivalent to the one in Ref. [21]:

$$\begin{aligned}\sigma_{\alpha\beta\gamma}(\omega) = \frac{ie^2}{\hbar}\sum_{l,n}\int [d\mathbf{k}]\Bigg\{&\frac{A_{\alpha,nl}\mathcal{T}_{\beta\gamma,ln} + A_{\beta,ln}\mathcal{T}_{\alpha\gamma,nl}}{\omega_{nl} + \omega + i\eta}f_{nl} \\ &- A_{\alpha,nl}A_{\beta,ln}\left(\frac{\omega\bar{f}_{\gamma,nl} + f_{nl}\bar{v}_{\gamma,nl}}{\omega_{nl}+\omega+i\eta} + \frac{\omega_{nl}f_{nl}\bar{v}_{\gamma,nl}}{(\omega_{nl}+\omega+i\eta)^2}\right)\Bigg\} \\ &+ \frac{e^2}{\hbar(\omega+i\eta)}\sum_n\int [d\mathbf{k}]\left(f_{\alpha,n}\mathcal{T}_{\beta\gamma,nn} - f_{\beta,n}\mathcal{T}_{\alpha\gamma,nn}\right) \\ &+ \frac{ie^2}{\hbar}\sum_n\int [d\mathbf{k}]g_{\alpha\beta,n}f_{\gamma,n} \\ &- \frac{ie^2}{\hbar(\omega+i\eta)^2}\sum_n\int [d\mathbf{k}]f'_n v_{\alpha,n}v_{\beta,n}v_{\gamma,n}.\end{aligned} \tag{13}$$

Here, e and $\hbar$ identify the elementary charge and the reduced Planck constant, respectively, $\int [d\mathbf{k}] = \int_{\mathrm{BZ}} d^3k/(2\pi)^3$, with the integral spanning the first Brillouin zone (BZ), and $\mathbf{k}$ dependence is implied in the integrands. $\omega_{nl} = \omega_n - \omega_l$ and $f_{nl} = f_n - f_l$ are interband frequencies and differences in occupation factors, respectively, and η is a positive infinitesimal. We have also defined

$$v_{\alpha,n} = \frac{\partial\omega_n}{\partial k_\alpha}, \tag{14a}$$

$$f'_n = \frac{\partial f_n}{\partial\omega_n}, \tag{14b}$$

$$f_{\alpha,n} = \frac{\partial f_n}{\partial k_\alpha} = f'_n v_{\alpha,n}, \tag{14c}$$

$$\bar{f}_{\alpha,nl} = \frac{1}{2}(f_{\alpha,n} + f_{\alpha,l}), \tag{14d}$$

$$\bar{v}_{\alpha,nl} = \frac{1}{2}(v_{\alpha,n} + v_{\alpha,l}). \tag{14e}$$

Tensors $A_{\alpha,ln}$ and $\mathcal{T}_{\alpha\beta,ln}$ containing optical matrix elements will be introduced below, along with the quantum-metric tensor $g_{\alpha\beta,n}$.

Every term in Eq. (13) except for the quantum-metric term has either one or two powers of $\omega + i\eta$ or $\omega_{nl} + \omega + i\eta$ in the denominator. Those terms with one power of frequency in the denominator give δ-like contributions to the optical absorption, and those with two give δ'-like contributions.

The first two lines of Eq. (13) contain the interband terms, and the last three describe the intraband terms. All intraband terms contain derivatives $\partial f/\partial k$ or $\partial f/\partial\omega$ and are thus Fermi-surface-like vanishing in the absence of free carriers. However, the reverse is not true: The term containing $\bar{f}_{\gamma,nl}$ in the second line is interband and Fermi-surface-like. In insulators and cold semiconductors only the first line and the two terms containing f_{nl} in the second line survive, while in molecules only the first line survives, as all other terms contain band velocities. The term in the last line, with a product of three band velocities, is Drude-like in the sense of depending only on the band structure.

All terms in the first two lines in Eq. (13) have both symmetric and antisymmetric parts in $\alpha\beta$; the third line is antisymmetric; and the fourth and the fifth are symmetric. Since the symmetric parts are time-odd, they vanish in the

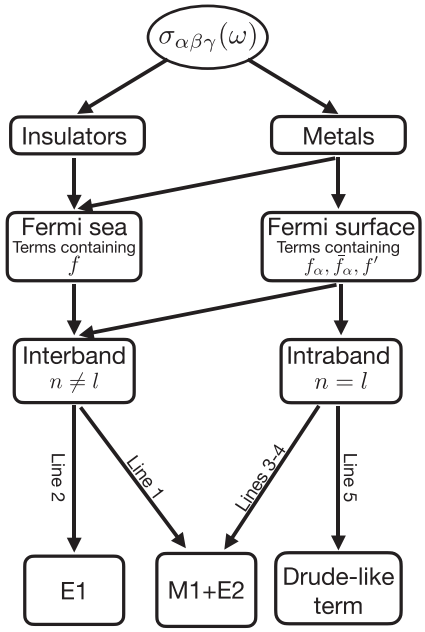

FIG. 1. Schematic chart of Eq. (13). The contributions to $\sigma_{\alpha\beta\gamma}$ are classified at three different levels according to whether they are (i) Fermi sea (bound carriers) or Fermi surface (free carriers), (ii) interband or intraband, and (iii) electric dipole (E1) or magnetic dipole plus electric quadrupole (M1 + E2). Terms containing the matrix $\mathcal{T}$ (see Fig. 2 below) are of the M1 + E2 type, whereas the E1 terms do not contain $\mathcal{T}$. The quantum-metric term is classified as E2, whereas the Drude-like term in the last line of Eq. (13) falls outside the E1-M1-E2 classification scheme.

presence of time-reversal symmetry. Thus, only the third line and the antisymmetric parts of the first two lines contribute in the case of nonmagnetic materials. For a nonmagnetic or collinear-spin system computed without spin-orbit coupling (SOC), the electron bands are all pure spin up or down, so that matrices indexed by ln are spin diagonal and Eq. (13) can be evaluated separately in each spin sector.

In Fig. 1, we provide a schematic summary to help the reader navigate Eq. (13) and classify all its terms.

The Hermitian matrices A_α and $\mathcal{T}_{\alpha\beta}$ contain the optical matrix elements at zeroth and first order in $\mathbf{q}$, respectively. A_α describes electric-dipole (E1) transitions, while $\mathcal{T}_{\alpha\beta}$ describes electric-quadrupole (E2) and magnetic-dipole (M1) transitions via its symmetric and antisymmetric parts, respectively (see Appendix A). A_α takes the form of a gauge-covariant Berry connection,

$$A_{\alpha,ln} = i\langle u_l|D_\alpha u_n\rangle, \tag{15}$$

with

$$|D_\alpha u_n\rangle = (1 - |u_n\rangle\langle u_n|)|\partial_\alpha u_n\rangle \tag{16}$$

the covariant derivative of a cell-periodic Bloch state $|u_n\rangle$, and $\partial_\alpha = \partial/\partial k_\alpha$ (here and throughout this section, we assume nondegenerate bands). While A_α is purely orbital and off-diagonal ($A_{\alpha,nn} = 0$), $\mathcal{T}_{\alpha\beta}$ has both orbital and spin parts, as well as diagonal and off-diagonal parts. It is given by

$$\mathcal{T}_{\alpha\beta,ln} = \frac{1}{2}(\mathcal{K}_{\alpha\beta,ln} + \mathcal{K}^*_{\alpha\beta,nl}) - \frac{g_s}{2m_e}\epsilon_{\alpha\beta\gamma}\mathcal{S}_{\gamma,ln}, \tag{17}$$

where in the first term the orbital matrix $\mathcal{K}_{\alpha\beta}$ reads

$$\mathcal{K}_{\alpha\beta,ln} = \frac{1}{i\hbar}\langle D_\alpha u_l|H - \epsilon_l|D_\beta u_n\rangle + v_{\alpha,l}A_{\beta,ln}, \tag{18}$$

and in the second $g_s \simeq 2$ is the spin g factor, m_e is the electron mass, and

$$\mathcal{S}_{\gamma,ln} = \frac{\hbar}{2}\langle u_l|\sigma_\gamma|u_n\rangle \tag{19}$$

is the spin matrix expressed in terms of Pauli matrices. The diagonal part of $\mathcal{T}_{\alpha\beta}$ appearing in the third line of Eq. (13) is purely antisymmetric (M1), while the off-diagonal part in the first line has both symmetric (E2) and antisymmetric (M1) components. Finally, the quantity

$$g_{\alpha\beta,n} = \mathrm{Re}\,\langle D_\alpha u_n|D_\beta u_n\rangle \tag{20}$$

in the fourth line of Eq. (13) is the single-band quantum metric [32,33]. It contributes a frequency-independent and purely reactive intraband response of E2 character.

We have adopted a notation where lower-case letters (f, g, v) are used for intraband quantities, and capital letters are used for matrices in the band indices; calligraphic letters ($\mathcal{K}$, $\mathcal{T}$, $\mathcal{S}$) are used for matrices with both interband and intraband parts, and Roman letters (A) for purely interband matrices. Intraband quantities can appear either as band vectors, like $v_{\alpha,n}$ and $g_{\alpha\beta,n}$, or as matrices, in which case they are automatically diagonal, e.g., $v_{\alpha,ln} = \delta_{ln}v_{\alpha,n}$.

The above quantities need to be computed on a sufficiently fine $\mathbf{k}$ mesh to obtain converged results for the optical responses of interest. We assume this is being done as a post-processing step after a self-consistent first-principles calculation. In the sum-over-states approach to be summarized in Sec. III, it is possible to compute the ingredients in Eqs. (15)–(20) directly, but with a limitation on the number of contributing conduction bands. To prepare for the Wannier interpolation approach to be introduced in Sec. IV, on the other hand, it is useful to define a set of auxiliary tensors from which these matrices can be constructed in a way that is free of the conduction-band limitation. These are introduced next.

C. Auxiliary matrices for Wannier interpolation

As we shall see in Sec. IV, our Wannier interpolation approach gives us convenient access to a set of auxiliary matrices

$$\mathcal{A}_{\alpha,ln} = i\langle u_l|\partial_\alpha u_n\rangle = \mathcal{A}^*_{\alpha,nl}, \tag{21a}$$

$$\mathcal{C}_{\alpha\beta,ln} = \langle \partial_\alpha u_l|\partial_\beta u_n\rangle = \mathcal{C}^*_{\beta\alpha,nl}, \tag{21b}$$

$$\mathcal{D}_{\alpha\beta,ln} = \langle \partial_\alpha u_l|H|\partial_\beta u_n\rangle = \mathcal{D}^*_{\beta\alpha,nl}. \tag{21c}$$

Here, we show how the $\mathcal{K}_{\alpha\beta}$ and $g_{\alpha\beta}$ tensors of Eqs. (18) and (20) can be obtained from these ingredients.

The Berry connection matrix can be decomposed into intraband and interband parts, $\mathcal{A}_\alpha = a_\alpha + A_\alpha$, with

$$a_{\alpha,ln} = \delta_{ln}\mathcal{A}_{\alpha,ln}, \tag{22a}$$

$$A_{\alpha,ln} = (1 - \delta_{ln})\mathcal{A}_{\alpha,ln}. \tag{22b}$$

A_α is the same as in Eq. (15), and the covariant derivative in Eq. (16) may now be written as

$$|D_\alpha u_n\rangle = |\partial_\alpha u_n\rangle + i|u_n\rangle a_{\alpha,n}, \tag{23}$$

where we have converted a_α to band-vector form. Inserting this expression in Eqs. (18) and (20) and then using Eq. (21) leads to

$$\mathcal{K}_{\alpha\beta,ln} = \frac{1}{i\hbar}(\mathcal{D}_{\alpha\beta,ln} - \epsilon_l \mathcal{C}_{\alpha\beta,ln}) - i\omega_{ln} A_{\alpha,ln} a_{\beta,n} + v_{\alpha,l} A_{\beta,ln} \tag{24}$$

and

$$g_{\alpha\beta,n} = \mathrm{Re}\, \mathcal{C}_{\alpha\beta,nn} - a_{\alpha,n} a_{\beta,n}. \tag{25}$$

Plugging Eq. (24) into Eq. (17) for $\mathcal{T}_{\alpha\beta}$ and invoking the Hermiticity relations in Eq. (21), one finds that the symmetric part of $\mathcal{D}_{\alpha\beta}$ drops out, so that $\mathcal{T}_{\alpha\beta}$ and $\sigma_{\alpha\beta\gamma}(\omega)$ only involve the antisymmetric part. Instead, both the symmetric and antisymmetric parts of $\mathcal{C}_{\alpha\beta}$ contribute; separating them as

$$\mathcal{C}_{\alpha\beta} = \frac{1}{2}(\mathcal{C}_{\alpha\beta} + \mathcal{C}_{\beta\alpha}) - \frac{i}{2}\mathcal{F}_{\alpha\beta} \tag{26}$$

where

$$\mathcal{F}_{\alpha\beta} = \partial_\alpha \mathcal{A}_\beta - \partial_\beta \mathcal{A}_\alpha \tag{27}$$

is the Abelian Berry curvature matrix, Eq. (24) becomes

$$\mathcal{K}_{\alpha\beta} = \frac{1}{i\hbar}\Big[\mathcal{D}_{\alpha\beta} - \frac{\epsilon}{2}(\mathcal{C}_{\alpha\beta} + \mathcal{C}_{\beta\alpha}) + \frac{i\epsilon}{2}\mathcal{F}_{\alpha\beta} + \epsilon A_\alpha a_\beta - A_\alpha a_\beta \epsilon\Big] + v_\alpha A_\beta, \tag{28}$$

where ϵ is the diagonal band-energy matrix and all products are matrix multiplications.

To recap, once the occupations f, band velocities v_α of Eq. (14a), and tensors $\mathcal{A}_\alpha$, $\mathcal{C}_{\alpha\beta}$, and $\mathcal{D}_{\alpha\beta}$ of Eq. (21) are available at a given **k** point, it is straightforward to compute, at that same point, the various quantities introduced above. The computation of these tensor ingredients needed for the Wannier-interpolation approach will be discussed in Sec. IV. Figure 2 presents a flowchart to summarize the important relationships to obtain the building blocks of the E1, M1, and E2 contributions to the optical conductivity in Eq. (13).

D. Summary

In this section, we have described the formalism and tensor ingredients needed to compute the spatial-dispersion conductivity tensor in Eq. (13). In the remainder of this paper, we first briefly describe a relatively straightforward sum-over-states approach for computing this conductivity, although it is not the one we have adopted. We then provide the details of our Wannier-interpolation approach and present some applications of this method.

III. SUM-OVER-STATES APPROACH

In this approach, one adopts a single **k** mesh for the entire calculation and computes the needed matrix elements directly from the Kohn-Sham wave functions on that mesh. The details are as follows.

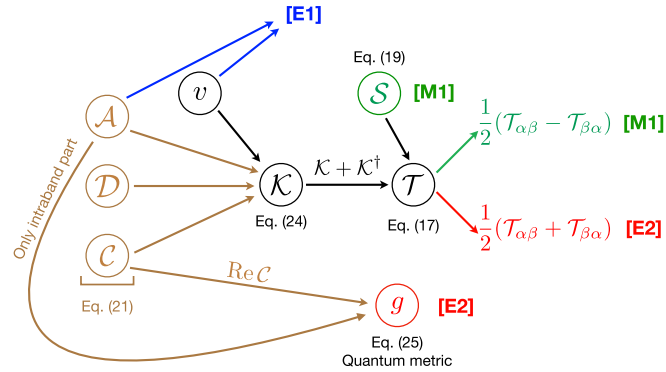

FIG. 2. Flowchart showing how the building blocks introduced in the main text are combined to obtain the electric dipole (E1, blue), magnetic dipole (M1, green) and electric quadrupole (E2, red) contributions to the spatially dispersive optical conductivity in Eq. (13). Quantities needed exclusively for the Wannier interpolation approach are highlighted in brown; the sum-over-states approach to the Kubo formulation requires only the velocity matrix elements and the interband frequencies (see Sec. III).

The spin matrices $\mathcal{S}_\gamma$ can be readily evaluated from Eq. (19). As for the orbital tensors A_α, $\mathcal{K}_{\alpha\beta}$, and $g_{\alpha\beta}$, they are evaluated via the sum-over-states expression for the covariant derivative (16),

$$|D_\alpha u_n\rangle = -\sum_{p\neq n} |u_p\rangle \frac{\mathcal{V}_{\alpha,pn}}{\omega_{pn}}. \tag{29}$$

Here,

$$\mathcal{V}_{\alpha,pn} = \frac{1}{\hbar}\langle u_p|(\partial_\alpha H)|u_n\rangle \tag{30}$$

is the velocity matrix, whose diagonal elements give the band velocity (14a),

$$v_{\alpha,n} = \mathcal{V}_{\alpha,nn}. \tag{31}$$

The orbital tensors can be written solely in terms of velocity matrix elements and interband frequencies. This can be seen by inserting Eq. (29) in Eqs. (15), (18), and (20), which gives

$$A_{\alpha,ln} = \begin{cases} \frac{\mathcal{V}_{\alpha,ln}}{i\omega_{ln}} & \text{if } l \neq n \\ 0 & \text{if } l = n \end{cases}, \tag{32}$$

$$\mathcal{K}_{\alpha\beta,ln} = (\mathcal{V}_\alpha A_\beta)_{ln}, \tag{33}$$

and

$$g_{\alpha\beta,n} = \mathrm{Re}(A_\alpha A_\beta)_{nn}. \tag{34}$$

To obtain Eq. (33), note the identity

$$\langle D_\alpha u_l|H - \epsilon_l|D_\beta u_n\rangle = i\hbar \sum_{p\neq l} \mathcal{V}_{\alpha,lp} A_{\beta,pn}, \tag{35}$$

which follows from Eqs. (15) and (29). Using that identity in Eq. (18) leads to

$$\mathcal{K}_{\alpha\beta,ln} = \sum_{p\neq l} \mathcal{V}_{\alpha,lp} A_{\beta,pn} + v_{\alpha,l} A_{\beta,ln} = \sum_{p} \mathcal{V}_{\alpha,lp} A_{\beta,pn} - \mathcal{V}_{\alpha,ll} A_{\beta,ln} + v_{\alpha,l} A_{\beta,ln}. \tag{36}$$

The last two terms cancel out, yielding Eq. (33).

The sum-over-states evaluation of $\sigma_{\alpha\beta\gamma}(\omega)$ was implemented in Ref. [20]. The advantage of this type of approach is the ease of implementation, especially if the *ab initio* code already provides the velocity matrix elements. One disadvantage is the need to truncate the implied summations over intermediate states in Eqs. (33) and (34). This can be traced back to a band-truncation error in the covariant derivative of Eq. (29), where index p only runs over the conduction bands carried in the first-principles calculation. It also suffers from the need to call the *ab initio* engine for every $\mathbf{k}$ when performing the BZ integral in Eq. (13), which can become costly for narrow-gap semiconductors and when evaluating Fermi-surface terms for conductors.

IV. WANNIER INTERPOLATION

To overcome the difficulties mentioned above, we adopt an approach based on Wannier interpolation [24–26]. As we shall see, some terms in the resulting expressions for A_α, $\mathcal{K}_{\alpha\beta}$, and $g_{\alpha\beta}$ resemble the sum-over-states formulas in Eqs. (32)–(34), while others resemble the k-derivative formulas in Eqs. (15), (20), and (28). This approach typically cannot treat as many interband excitations as is allowed by the sum-over-states approach. However, it is free from band-truncation errors in the computation of optical matrix elements, and it allows the optical properties to be calculated efficiently on a fine interpolation mesh of $\mathbf{k}$ points.

A. Basics of Wannier interpolation

The Wannier functions (WFs) are constructed as

$$|\mathbf{R}j\rangle = \frac{1}{N}\sum_{\mathbf{q}} e^{-i\mathbf{q}\cdot(\mathbf{R}+\boldsymbol{\tau}_j)}\big|\psi^{\mathrm{W}}_{j\mathbf{q}}\big\rangle \quad (j=1,\ldots,M), \tag{37}$$

where $\mathbf{R}$ is a Bravais lattice vector and

$$\big|\psi^{\mathrm{W}}_{j\mathbf{q}}\big\rangle = \sum_n |\psi_{n\mathbf{q}}\rangle \mathcal{W}_{nj}(\mathbf{q}). \tag{38}$$

The summation in Eq. (37) is over the uniform Brillouin-zone mesh of N points $\mathbf{q}$ where the *ab initio* Bloch eigenstates $|\psi_{n\mathbf{q}}\rangle$ were calculated, and the Wannier-gauge Bloch-like states $|\psi^{\mathrm{W}}_{j\mathbf{q}}\rangle$ are related to the Bloch eigenstates by a unitary wannierization matrix $\mathcal{W}(\mathbf{q})$. That matrix is $M\times M$ without disentanglement [33], and with disentanglement it becomes $J(\mathbf{q})\times M$ with $J(\mathbf{q})\geqslant M$ at every $\mathbf{q}$ [34]. Since in WANNIER90 [35] the Wannier centers $\boldsymbol{\tau}_j = \langle \mathbf{0}j|\mathbf{r}|\mathbf{0}j\rangle$ are not included in the Fourier phase factors, $\mathcal{W}(\mathbf{q})$ in Eq. (38) is related to WANNIER90's wannierization matrix $\tilde{\mathcal{W}}(\mathbf{q})$ by

$$\mathcal{W}_{nj}(\mathbf{q}) = \tilde{\mathcal{W}}_{nj}(\mathbf{q})\, e^{i\mathbf{q}\cdot\boldsymbol{\tau}_j}. \tag{39}$$

Once the WFs have been constructed using a relatively coarse $\mathbf{q}$ grid, a Bloch basis is defined at each point $\mathbf{k}$ on the dense interpolation grid as

$$\big|\psi^{\mathrm{W}}_{j\mathbf{k}}\big\rangle = \sum_{\mathbf{R}} e^{i\mathbf{k}\cdot(\mathbf{R}+\boldsymbol{\tau}_j)}|\mathbf{R}j\rangle. \tag{40}$$

Here the sum over $\mathbf{R}$ is restricted such that $|\mathbf{R}j\rangle$ lies inside the Wigner-Seitz cell of the supercell conjugate to the coarse $\mathbf{q}$ grid [36]. The Hamiltonian matrix in this basis reads

$$\mathcal{H}^{\mathrm{W}}_{ij}(\mathbf{k}) = \big\langle u^{\mathrm{W}}_{i\mathbf{k}}\big|H_{\mathbf{k}}\big|u^{\mathrm{W}}_{j\mathbf{k}}\big\rangle, \tag{41}$$

where we have switched to cell-periodic states and defined $H_{\mathbf{k}} = e^{-i\mathbf{k}\cdot\mathbf{r}}He^{i\mathbf{k}\cdot\mathbf{r}}$. To obtain the interpolated band energies [38], the matrix $\mathcal{H}^{\mathrm{W}}$ is diagonalized as

$$\mathcal{H}^{\mathrm{H}}_{ln}(\mathbf{k}) = [\mathcal{U}^\dagger(\mathbf{k})\mathcal{H}^{\mathrm{W}}(\mathbf{k})\mathcal{U}(\mathbf{k})]_{ln} = \delta_{ln}\epsilon_{n\mathbf{k}}, \tag{42}$$

where $\mathcal{U}(\mathbf{k})$ is a unitary matrix and the H superscript stands for Hamiltonian gauge. (When disentanglement is not used, $\mathcal{U}=\mathcal{W}^\dagger$ on mesh points $\mathbf{k}=\mathbf{q}$.)

Equation (42) can be brought to the same form as Eq. (41) by defining

$$\big|u^{\mathrm{H}}_{n\mathbf{k}}\big\rangle = \sum_j \big|u^{\mathrm{W}}_{j\mathbf{k}}\big\rangle \mathcal{U}_{jn}(\mathbf{k}), \tag{43}$$

so that

$$\mathcal{H}^{\mathrm{H}}_{ln}(\mathbf{k}) = \big\langle u^{\mathrm{H}}_{l\mathbf{k}}\big|H_{\mathbf{k}}\big|u^{\mathrm{H}}_{n\mathbf{k}}\big\rangle = \delta_{ln}\epsilon_{n\mathbf{k}}. \tag{44}$$

Differentiating Eq. (43) gives (from now on we drop $\mathbf{k}$)

$$\big|\partial_\alpha u^{\mathrm{H}}_n\big\rangle = \sum_j \big|\partial_\alpha u^{\mathrm{W}}_j\big\rangle \mathcal{U}_{jn} - i\sum_l \big|u^{\mathrm{H}}_l\big\rangle \mathcal{A}^{\mathrm{I}}_{\alpha,ln}, \tag{45}$$

where

$$\mathcal{A}^{\mathrm{I}}_\alpha = i\mathcal{U}^\dagger\partial_\alpha\mathcal{U} \tag{46}$$

is the Berry connection matrix constructed from derivatives of the column vectors of $\mathcal{U}$ (the eigenvectors of $\mathcal{H}^{\mathrm{W}}$). We refer to quantities of this kind, which can be expressed solely in terms of the $M\times M$ Wannier Hamiltonian matrix $\mathcal{H}^{\mathrm{W}}(\mathbf{k})$ and its M-component column eigenvectors $\mathcal{U}(\mathbf{k})$, as *internal* (I). Instead, *external* (E) quantities are those that depend on the character of the Wannier functions themselves relative to the full Hilbert space. Considering only the internal terms is equivalent to treating the problem at a tight-binding level in the Wannier subspace, with on-site energies, hoppings, and orbital centers as the only model parameters. The external terms capture the extra embedding information that is missed by the standard tight-binding description. This partition becomes particularly clear and meaningful when the intracell Wannier centers $\boldsymbol{\tau}_j$ are included in the Fourier phase factors, as done in Eqs. (37) and (40).

Using Eq. (45) in Eq. (21a) for $\mathcal{A}_\alpha$ yields the Hamiltonian-gauge Berry connection [24]

$$\mathcal{A}^{\mathrm{H}}_\alpha = \mathcal{A}^{\mathrm{I}}_\alpha + \mathcal{A}^{\mathrm{E}}_\alpha, \tag{47}$$

where the external part reads

$$\mathcal{A}^{\mathrm{E}}_\alpha = \mathcal{U}^\dagger\mathcal{A}^{\mathrm{W}}_\alpha\mathcal{U} \tag{48}$$

with

$$\mathcal{A}^{\mathrm{W}}_{\alpha,ij} = i\big\langle u^{\mathrm{W}}_i\big|\partial_\alpha u^{\mathrm{W}}_j\big\rangle. \tag{49}$$

More generally, for any Wannier-gauge matrix $\mathcal{O}^{\mathrm{W}}$ we define its external part to be

$$\mathcal{O}^{\mathrm{E}} = \mathcal{U}^\dagger\mathcal{O}^{\mathrm{W}}\mathcal{U}, \tag{50}$$

and when $\mathcal{O}^{\mathrm{H}} = \mathcal{O}^{\mathrm{E}}$ that matrix is said to be gauge covariant [24]. In view of Eqs. (42) and (47), we conclude that $\mathcal{H}$ is gauge covariant but $\mathcal{A}_\alpha$ is not.

We are now ready to evaluate the covariant derivative (16) of an interpolated Bloch state $|u^{\mathrm{H}}_n\rangle$. Multiplying by $1-$

$|u_n^{\mathrm{H}}\rangle\langle u_n^{\mathrm{H}}|$ on both sides of Eq. (45) yields

$$|D_\alpha u_n^{\mathrm{H}}\rangle = \sum_j |\partial_\alpha u_j^{\mathrm{W}}\rangle \mathcal{U}_{jn} + i|u_n^{\mathrm{H}}\rangle a^{\mathrm{E}}_{\beta,n} - i\sum_p |u_p^{\mathrm{H}}\rangle A^{\mathrm{I}}_{\alpha,pn} \tag{51}$$

where, by analogy with Eq. (22), a^{E} is the intraband part of $\mathcal{A}^{\mathrm{E}}$ and A^{I} is the interband part of $\mathcal{A}^{\mathrm{I}}$. Note that this expression for $|D_\alpha u_n^{\mathrm{H}}\rangle$ does not suffer from the same band-truncation error as was discussed above for the sum-over-states approach: see Eq. (29). Here, the covariant derivative has the full accuracy of the plane-wave (or other first-principles) basis, as do the various tensors computed from it.

B. Application to $\sigma_{\alpha\beta\gamma}(\omega)$

1. Optical matrix elements

In Sec. III, the optical matrix elements entering Eq. (13) for $\sigma_{\alpha\beta\gamma}$ were evaluated using the sum-over-states formula of Eq. (29) for $|D_\alpha u_n\rangle$. In our approach we evaluate the covariant derivatives using Eq. (51) instead. Our immediate goal is to obtain the needed quantities such as A_α of Eq. (15) and $\mathcal{K}_{\alpha\beta}$ of Eq. (18) on a coarse $\mathbf{q}$ mesh. These will then be Wannier interpolated onto a fine $\mathbf{k}$ mesh as described in detail later in Sec. IV B 3.

The covariant derivatives $|D_\alpha u_n\rangle$ are not needed for the Hamiltonian and spin matrices, which can be obtained directly from the first-principles calculation as in Sec. III. For consistency with what follows, however, we transform them to the Wannier gauge using Eq. (38) to obtain

$$\mathcal{H}^{\mathrm{W}}_{ij} = \langle u_i^{\mathrm{W}}|H|u_j^{\mathrm{W}}\rangle, \tag{52a}$$

$$\mathcal{S}^{\mathrm{W}}_{\alpha,ij} = \langle u_i^{\mathrm{W}}|S_\alpha|u_j^{\mathrm{W}}\rangle. \tag{52b}$$

We then also construct a set of Wannier-gauge orbital matrices

$$\mathcal{A}^{\mathrm{W}}_{\alpha,ij} = i\langle u_i^{\mathrm{W}}|\partial_\alpha u_j^{\mathrm{W}}\rangle, \tag{53a}$$

$$\mathcal{B}^{\mathrm{W}}_{\alpha,ij} = i\langle u_i^{\mathrm{W}}|H|\partial_\alpha u_j^{\mathrm{W}}\rangle, \tag{53b}$$

$$\mathcal{C}^{\mathrm{W}}_{\alpha\beta,ij} = \langle \partial_\alpha u_i^{\mathrm{W}}|\partial_\beta u_j^{\mathrm{W}}\rangle, \tag{53c}$$

$$\mathcal{D}^{\mathrm{W}}_{\alpha\beta,ij} = \langle \partial_\alpha u_i^{\mathrm{W}}|H|\partial_\beta u_j^{\mathrm{W}}\rangle \tag{53d}$$

on the coarse mesh. The derivatives in these equations are evaluated by finite differences on the coarse $\mathbf{q}$ mesh as described in Sec. IV B 2; this has to be done in the Wannier gauge to enforce a smooth evolution of wave functions between neighboring $\mathbf{q}$ points. After Wannier interpolation of the quantities in Eqs. (52) and (53) onto the fine $\mathbf{k}$ mesh, it is relatively straightforward to compute quantities such as those in Eqs. (15) and (18) in the Hamiltonian gauge, as described below.

In Eq. (53), compared to Eq. (21), we have introduced an additional matrix $\mathcal{B}_\alpha$, which will be needed later in the interpolation formula for $\mathcal{K}_{\alpha\beta}$ if Wannier disentanglement is used. Recall from Eq. (21) that $\mathcal{A}_\alpha$, $\mathcal{C}_{\alpha\beta}$, and $\mathcal{D}_{\alpha\beta}$ satisfy Hermiticity relations. Instead, $\mathcal{B}_\alpha$ satisfies the generalized Hermiticity constraint

$$\left(\mathcal{B}^{\mathrm{W}}_{\alpha,ji}\right)^* = \mathcal{B}^{\mathrm{W}}_{\alpha,ij} + i\hbar\mathcal{V}^{\mathrm{W}}_{\alpha,ij} - i\partial_\alpha \mathcal{H}^{\mathrm{W}}_{ij}, \tag{54}$$

which follows from differentiating Eq. (41) for $\mathcal{H}^{\mathrm{W}}$, with $\mathcal{V}_\alpha$ given by Eq. (30). Following Eq. (27), we also define

$$\mathcal{F}^{\mathrm{W}}_{\alpha\beta} = \partial_\alpha \mathcal{A}^{\mathrm{W}}_\beta - \partial_\beta \mathcal{A}^{\mathrm{W}}_\alpha. \tag{55}$$

As a reminder, our goal is to obtain the quantities A_α, $\mathcal{K}_{\alpha\beta}$, $g_{\alpha\beta}$, and S_α in the Hamiltonian gauge from the above Wannier-gauge matrices. Let us start with the spin matrix in Eq. (19). Using Eq. (43) we find

$$\mathcal{S}^{\mathrm{H}}_\alpha = \mathcal{U}^\dagger \mathcal{S}^{\mathrm{W}}_\alpha \mathcal{U} = \mathcal{S}^{\mathrm{E}}_\alpha. \tag{56}$$

Thus, the $\mathcal{S}_\alpha$ matrix is gauge covariant, just like $\mathcal{H}$. But while $\mathcal{H}^{\mathrm{H}}$ in Eq. (42) is diagonal by construction, $\mathcal{S}^{\mathrm{H}}_\alpha$ is generally nondiagonal in the presence of SOC.

The orbital matrices A_α, $\mathcal{K}_{\alpha\beta}$, and $g_{\alpha\beta}$, on the other hand, are noncovariant (i.e., they are not equal to their external parts). For example, inserting Eq. (51) in Eq. (15) for A_α gives

$$A^{\mathrm{H}}_\alpha = A^{\mathrm{I}}_\alpha + A^{\mathrm{E}}_\alpha, \tag{57a}$$

$$A^{\mathrm{I}}_{\alpha,ln} \equiv (1-\delta_{ln})\mathcal{A}^{\mathrm{I}}_{\alpha,ln} = \begin{cases} \frac{\mathcal{V}^{\mathrm{I}}_{\alpha,ln}}{i\omega_{ln}} & \text{if } l \neq n \\ 0 & \text{if } l = n \end{cases}, \tag{57b}$$

$$A^{\mathrm{E}}_{\alpha,ln} \equiv (1-\delta_{ln})\mathcal{A}^{\mathrm{E}}_{\alpha,ln} = (1-\delta_{ln})\left[\mathcal{U}^\dagger \mathcal{A}^{\mathrm{W}}_\alpha \mathcal{U}\right]_{ln}. \tag{57c}$$

In Eq. (57b) $\mathcal{V}^{\mathrm{I}}_\alpha$ is the internal velocity matrix

$$\mathcal{V}^{\mathrm{I}}_\alpha = \frac{1}{\hbar}\mathcal{U}^\dagger(\partial_\alpha \mathcal{H}^{\mathrm{W}})\mathcal{U}, \tag{58}$$

and the right-hand side of Eq. (57c) follows from Eq. (48) for $\mathcal{A}^{\mathrm{E}}_\alpha$. Note that Eqs. (57b) and (58) have the same form as Eqs. (32) and (30) for A_α and $\mathcal{V}_\alpha$, except that they are written in terms of internal quantities. Moreover, the interpolated band velocities can be obtained from Eq. (58) via the internal analogue of Eq. (31),

$$v_{\alpha,n} = \mathcal{V}^{\mathrm{I}}_{\alpha,nn}. \tag{59}$$

Using Eq. (51) in Eq. (18) for $\mathcal{K}_{\alpha\beta}$ one finds (see Appendix B) that it contains not only internal and external terms, but also *cross* (X) terms that mix internal and external quantities,

$$\mathcal{K}^{\mathrm{H}}_{\alpha\beta} = \mathcal{K}^{\mathrm{I}}_{\alpha\beta} + \mathcal{K}^{\mathrm{E}}_{\alpha\beta} + \mathcal{K}^{\mathrm{X}}_{\alpha\beta}, \tag{60a}$$

$$\mathcal{K}^{\mathrm{I}}_{\alpha\beta} = \mathcal{V}^{\mathrm{I}}_\alpha A^{\mathrm{I}}_\beta, \tag{60b}$$

$$\mathcal{K}^{\mathrm{E}}_{\alpha\beta} = \frac{1}{i\hbar}\Big[\mathcal{D}^{\mathrm{E}}_{\alpha\beta} - \frac{\epsilon}{2}\left(\mathcal{C}^{\mathrm{E}}_{\alpha\beta} + \mathcal{C}^{\mathrm{E}}_{\beta\alpha}\right) + \frac{i\epsilon}{2}\mathcal{F}^{\mathrm{E}}_{\alpha\beta} + \epsilon A^{\mathrm{E}}_\alpha a^{\mathrm{E}}_\beta - A^{\mathrm{E}}_\alpha a^{\mathrm{E}}_\beta \epsilon\Big] + v_\alpha A^{\mathrm{E}}_\beta, \tag{60c}$$

$$\mathcal{K}^{\mathrm{X}}_{\alpha\beta} = \frac{1}{i\hbar}\Big[A^{\mathrm{I}}_\alpha B^{\mathrm{E}}_\beta - \epsilon A^{\mathrm{I}}_\alpha A^{\mathrm{E}}_\beta + \left(A^{\mathrm{I}}_\beta B^{\mathrm{E}}_\alpha - A^{\mathrm{I}}_\beta A^{\mathrm{E}}_\alpha \epsilon\right)^\dagger\Big]. \tag{60d}$$

Here, $\epsilon = \mathcal{H}^{\mathrm{H}}$ and v_α are the diagonal band-energy and band-velocity matrices, respectively, and B^{E}_α is the off-diagonal part of $\mathcal{B}^{\mathrm{E}}_\alpha$. Equation (60b) is the internal analog of the sum-over-states formula (33) for $\mathcal{K}_{\alpha\beta}$, and Eq. (60c) is the external analog of the k-derivative formula (28).

When disentanglement is not used in the Wannier construction, Eq. (60d) can be simplified using the relation

$$\mathcal{B}^{\mathrm{E}}_{\alpha,ln} = \epsilon_l \mathcal{A}^{\mathrm{E}}_{\alpha,ln} \tag{61}$$

from Appendix B. This is an exact identity when the interpolation point falls on the *ab initio* mesh and an excellent approximation otherwise. In this case, Eq. (60d) reduces to

$$\mathcal{K}^{\mathrm{X}}_{\alpha\beta} = \frac{1}{i\hbar}\big[A^{\mathrm{I}}_\alpha \epsilon A^{\mathrm{E}}_\beta - \epsilon A^{\mathrm{I}}_\alpha A^{\mathrm{E}}_\beta + (\mathrm{I} \leftrightarrow \mathrm{E})\big], \tag{62}$$

which further highlights the parallelism with the sum-over-states formula (33) for $\mathcal{K}_{\alpha\beta}$. Of course, the optical absorption spectra predicted from $\mathcal{K}^{\mathrm{H}}_{\alpha\beta,ln}$ can only cover the frequency range of transitions between wannierized bands l and n.

When disentanglement is used, we make the same assumption about the range of computed spectra, but now insisting that bands l and n lie inside the frozen window. In this case, Eq. (60) is still correct as written, but the replacement of Eq. (60d) by Eq. (62) is no longer justified when the interior band index (p in an expression like $\sum_p A^{\mathrm{I}}_{\alpha,lp} B^{\mathrm{E}}_{\beta,pn}$) lies outside the frozen window. While Eq. (60d) could be used for both situations, we find it convenient to use Eq. (62) when p lies in the frozen window and Eq. (60d) otherwise [39].

Since l and n must lie inside the frozen window, the sums in the Kubo formula (13) for the optical conductivity are restricted to a subset of the *ab initio* bands. This leads to a truncation error, inherent to the present methodology, which can be controlled by enlarging the frozen window to capture the relevant conduction states. This truncation error affects only the reactive part of the response; the absorptive part is not affected because, as noted in Sec. II B, it comes with $\delta(\omega_{nl} - \omega)$ and $\delta'(\omega_{nl} - \omega)$ factors, which restrict the sums over l and n to a small subset of states close to the optical transition.

Finally, using Eq. (51) in Eq. (20) gives for the quantum metric

$$g^{\mathrm{H}}_{\alpha\beta,n} = g^{\mathrm{I}}_{\alpha\beta,n} + g^{\mathrm{E}}_{\alpha\beta,n} + g^{\mathrm{X}}_{\alpha\beta,n}, \tag{63a}$$

$$g^{\mathrm{I}}_{\alpha\beta,n} = \mathrm{Re}\big(A^{\mathrm{I}}_\alpha A^{\mathrm{I}}_\beta\big)_{nn}, \tag{63b}$$

$$g^{\mathrm{E}}_{\alpha\beta,n} = \mathrm{Re}\, \mathcal{C}^{\mathrm{E}}_{\alpha\beta,nn} - a^{\mathrm{E}}_{\alpha,n} a^{\mathrm{E}}_{\beta,n}, \tag{63c}$$

$$g^{\mathrm{X}}_{\alpha\beta,n} = \mathrm{Re}\big(A^{\mathrm{I}}_\alpha A^{\mathrm{E}}_\beta + A^{\mathrm{E}}_\alpha A^{\mathrm{I}}_\beta\big)_{nn}. \tag{63d}$$

Equation (63b) is the internal counterpart of the sum-over-states formula (34) for $g_{\alpha\beta,n}$, and Eq. (63c) is the external counterpart of the k-derivative formula (25); as in the case of $\mathcal{K}_{\alpha\beta}$, the cross term is similar to the internal term and to the sum-over-states expression.

In summary, the interpolated spin matrix is given by Eq. (56); of the three orbital matrices entering Eq. (13), A_α [Eq. (57)] contains only internal and external terms in the Wannier representation, while $\mathcal{K}_{\alpha\beta}$ [Eq. (60)] and $g_{\alpha\beta}$ [Eq. (63)] also contain cross terms. The band energies and band velocities appearing in Eq. (60) and elsewhere in Eq. (13) are obtained from Eqs. (42) and (59), respectively, with Eq. (42) also providing the $\mathcal{U}$ matrices.

The only remaining task is to compute the Wannier-gauge matrices in Eqs. (52) and (53). The derivatives with respect to wave vector in Eq. (53) will be evaluated by finite differences on the coarse $\mathbf{q}$ mesh as described in the next section. At this point, if we were only interested in computing the responses on the coarse mesh, we would essentially be done. However, one of the main advantages of the Wannier interpolation approach is that it now allows these matrices to be interpolated efficiently onto a fine mesh for a higher-resolution calculation of the optical response, as described in Sec. IV B 3.

2. Construction of Wannier-gauge matrices

To interpolate the Wannier-gauge matrices $\mathcal{O}^{\mathrm{W}}$, with $\mathcal{O} = \mathcal{H}, \mathcal{S}_\alpha, \mathcal{A}_\alpha, \mathcal{B}_\alpha, \mathcal{C}_{\alpha\beta}, \mathcal{D}_{\alpha\beta}$, onto a fine mesh of $\mathbf{k}$ points, one needs first to compute $\mathcal{O}^{\mathrm{W}}$ on the coarse *ab initio* $\mathbf{q}$ mesh. This is done starting from Eq. (52) for the Hamiltonian and spin matrices and from Eq. (53) for the orbital matrices, and using Eq. (38). In particular, the derivatives appearing in Eq. (53) are computed by finite differences on the $\mathbf{q}$ grid as [33]

$$\big|\partial_\alpha u^{\mathrm{W}}_{j\mathbf{q}}\big\rangle \simeq \sum_{\mathbf{b}} w_b b_\alpha \big|u^{\mathrm{W}}_{j\mathbf{q}+\mathbf{b}}\big\rangle, \tag{64}$$

where w_b are appropriately chosen weights, and the sum is performed over shells of vectors $\mathbf{b}$ connecting a point $\mathbf{q}$ of the *ab initio* grid to its neighbors. In this way, the Wannier-gauge Hamiltonian and spin matrices in the coarse $\mathbf{q}$ mesh read

$$\mathcal{H}^{\mathrm{W}}(\mathbf{q}) = \mathcal{W}^\dagger(\mathbf{q}) \mathbb{H}(\mathbf{q}) \mathcal{W}(\mathbf{q}), \tag{65a}$$

$$\mathcal{S}^{\mathrm{W}}_\alpha(\mathbf{q}) = \mathcal{W}^\dagger(\mathbf{q}) \mathbb{S}_\alpha(\mathbf{q}) \mathcal{W}(\mathbf{q}), \tag{65b}$$

whereas the orbital matrices take the form

$$\mathcal{A}^{\mathrm{W}}_{\alpha,ij}(\mathbf{q}) \simeq i \sum_{\mathbf{b}} w_b b_\alpha [\mathcal{W}^\dagger(\mathbf{q}) \mathbb{M}(\mathbf{q}, \mathbf{q}+\mathbf{b}) \mathcal{W}(\mathbf{q}+\mathbf{b})]_{ij}, \tag{66a}$$

$$\mathcal{B}^{\mathrm{W}}_{\alpha,ij}(\mathbf{q}) \simeq i \sum_{\mathbf{b}} w_b b_\alpha [\mathcal{W}^\dagger(\mathbf{q}) \mathbb{H}(\mathbf{q}) \mathbb{M}(\mathbf{q}, \mathbf{q}+\mathbf{b}) \times \mathcal{W}(\mathbf{q}+\mathbf{b})]_{ij}, \tag{66b}$$

$$\mathcal{C}^{\mathrm{W}}_{\alpha\beta,ij}(\mathbf{q}) \simeq \sum_{\mathbf{b},\mathbf{b}'} w_b w_{b'} b_\alpha b'_\beta [\mathcal{W}^\dagger(\mathbf{q}+\mathbf{b}) \mathbb{M}(\mathbf{q}+\mathbf{b}, \mathbf{q}+\mathbf{b}') \times \mathcal{W}(\mathbf{q}+\mathbf{b}')]_{ij}, \tag{66c}$$

$$\mathcal{D}^{\mathrm{W}}_{\alpha\beta,ij}(\mathbf{q}) \simeq \sum_{\mathbf{b},\mathbf{b}'} w_b w_{b'} b_\alpha b'_\beta [\mathcal{W}^\dagger(\mathbf{q}+\mathbf{b}) \mathbb{N}(\mathbf{q}+\mathbf{b}, \mathbf{q}+\mathbf{b}') \times \mathcal{W}(\mathbf{q}+\mathbf{b}')]_{ij}. \tag{66d}$$

Here, $\mathcal{W}(\mathbf{q})$ is related by Eq. (39) to the $\tilde{\mathcal{W}}(\mathbf{q})$ matrix provided by WANNIER90, and

$$\mathbb{H}_{mn}(\mathbf{q}) = \langle u_{m\mathbf{q}} | H_{\mathbf{q}} | u_{n\mathbf{q}} \rangle = \delta_{mn} \epsilon_{n\mathbf{q}}, \tag{67a}$$

$$\mathbb{S}_{\alpha,mn}(\mathbf{q}) = \langle u_{m\mathbf{q}} | S_\alpha | u_{n\mathbf{q}} \rangle, \tag{67b}$$

TABLE I. Quantities needed from the *ab initio* code to evaluate Eq. (13) by Wannier interpolation. The filename convention follows PW2WANNIER90, the interface between the *ab initio* code QUANTUM ESPRESSO [40,41] and WANNIER90.

Ab initio matrix	Needed for	Stored in
$\mathbb{H}(\mathbf{q}) = \langle u_\mathbf{q}\|H_\mathbf{q}\|u_\mathbf{q}\rangle$	$\mathcal{H}^\mathrm{W}(\mathbf{q})$, $\mathcal{B}^\mathrm{W}_\alpha(\mathbf{q})$	`seedname.eig`
$\mathbb{S}_\alpha(\mathbf{q}) = \langle u_\mathbf{q}\|S_\alpha\|u_\mathbf{q}\rangle$	$\mathcal{S}^\mathrm{W}_\alpha(\mathbf{q})$	`seedname.spn`
$\mathbb{M}(\mathbf{q}, \mathbf{q}+\mathbf{b}) = \langle u_\mathbf{q}\|u_{\mathbf{q}+\mathbf{b}}\rangle$	$\mathcal{A}^\mathrm{W}_\alpha(\mathbf{q})$, $\mathcal{B}^\mathrm{W}_\alpha(\mathbf{q})$	`seedname.mmn`
$\mathbb{M}(\mathbf{q}+\mathbf{b}, \mathbf{q}+\mathbf{b}') = \langle u_{\mathbf{q}+\mathbf{b}}\|u_{\mathbf{q}+\mathbf{b}'}\rangle$	$\mathcal{C}^\mathrm{W}_{\alpha\beta}(\mathbf{q})$	`seedname.uIu`
$\mathbb{N}(\mathbf{q}+\mathbf{b}, \mathbf{q}+\mathbf{b}') = \langle u_{\mathbf{q}+\mathbf{b}}\|H_\mathbf{q}\|u_{\mathbf{q}+\mathbf{b}'}\rangle$	$\mathcal{D}^\mathrm{W}_{\alpha\beta}(\mathbf{q})$	`seedname.uHu`

$$\mathbb{M}_{mn}(\mathbf{q}, \mathbf{q}+\mathbf{b}) = \langle u_{m\mathbf{q}}|u_{n,\mathbf{q}+\mathbf{b}}\rangle, \tag{67c}$$

$$\mathbb{M}_{mn}(\mathbf{q}+\mathbf{b}, \mathbf{q}+\mathbf{b}') = \langle u_{m,\mathbf{q}+\mathbf{b}}|u_{n,\mathbf{q}+\mathbf{b}'}\rangle, \tag{67d}$$

$$\mathbb{N}_{mn}(\mathbf{q}+\mathbf{b}, \mathbf{q}+\mathbf{b}') = \langle u_{m,\mathbf{q}+\mathbf{b}}|H_\mathbf{q}|u_{n,\mathbf{q}+\mathbf{b}'}\rangle, \tag{67e}$$

are matrices provided by the *ab initio* code through its interface to WANNIER90. This complete list of *ab initio* matrices, which are needed to compute $\sigma_{\alpha\beta\gamma}$, is also summarized in Table I.

Compared to the ground-state bulk magnetization [26], an additional piece of information [Eq. (67d)], stored in the `seedname.uIu` file, is required. According to Eqs. (17) and (60c), that information is only used for the symmetric (E2) part of the $\mathcal{T}_{\alpha\beta}$ matrix, not for the antisymmetric (M1) part. Conversely, the information stored in `seedname.uHu` [Eq. (67e)] is only used for the antisymmetric part of $\mathcal{T}_{\alpha\beta}$; this is due to the fact that the symmetric part of $\mathcal{D}_{\alpha\beta}$ drops out from $\mathcal{T}_{\alpha\beta}$, as discussed in Sec. II C.

3. *Wannier interpolation onto the fine mesh*

Once the matrices on the $\mathbf{q}$ mesh are computed, they are Fourier-interpolated onto a finer mesh in the following way. First, a Fourier transform to real space is performed,

$$\mathcal{O}_{ij}(\mathbf{R}) = \frac{1}{N}\sum_\mathbf{q} e^{-i\mathbf{q}\cdot(\mathbf{R}+\boldsymbol{\tau}_j-\boldsymbol{\tau}_i)}\mathcal{O}^\mathrm{W}_{ij}(\mathbf{q}), \tag{68}$$

then, the real space matrices are Fourier transformed to the fine $\mathbf{k}$ mesh,

$$\mathcal{O}^\mathrm{W}_{ij}(\mathbf{k}) = \sum_\mathbf{R} e^{i\mathbf{k}\cdot(\mathbf{R}+\boldsymbol{\tau}_j-\boldsymbol{\tau}_i)}\mathcal{O}_{ij}(\mathbf{R}). \tag{69}$$

In these expressions, $\mathcal{O}_{ij}(\mathbf{R}) = \langle \mathbf{0}i|\mathcal{O}|\mathbf{R}j\rangle$. The real-space matrix elements of $\mathcal{H}$ and $\mathcal{S}_\alpha$ read

$$\mathcal{H}_{ij}(\mathbf{R}) = \langle \mathbf{0}i|H|\mathbf{R}j\rangle, \tag{70a}$$

$$\mathcal{S}_{\alpha,ij}(\mathbf{R}) = \langle \mathbf{0}i|S_\alpha|\mathbf{R}j\rangle, \tag{70b}$$

whereas those of the orbital matrices are

$$\mathcal{A}_{\alpha,ij}(\mathbf{R}) = \langle \mathbf{0}i|(r-R-\tau_j)_\alpha|\mathbf{R}j\rangle, \tag{71a}$$

$$\mathcal{B}_{\alpha,ij}(\mathbf{R}) = \langle \mathbf{0}i|H(r-R-\tau_j)_\alpha|\mathbf{R}j\rangle, \tag{71b}$$

$$\mathcal{C}_{\alpha\beta,ij}(\mathbf{R}) = \langle \mathbf{0}i|(r-\tau_i)_\alpha(r-R-\tau_j)_\beta|\mathbf{R}j\rangle, \tag{71c}$$

$$\mathcal{D}_{\alpha\beta,ij}(\mathbf{R}) = \langle \mathbf{0}i|(r-\tau_i)_\alpha H(r-R-\tau_j)_\beta|\mathbf{R}j\rangle. \tag{71d}$$

Equation (69) concludes the Wannier interpolation. Once the Wannier-gauge matrices are known on the fine mesh, they are used to compute the optical matrix elements in the Hamiltonian gauge via the interpolation formulas obtained in Sec. IV B 1. To this end, we note that the internal velocity $\mathcal{V}^\mathrm{I}_\alpha$ is also needed, particularly to compute the internal parts of the Berry connection [Eq. (57b)] and of $\mathcal{K}_{\alpha\beta}$ [Eq. (60b)]. To evaluate $\mathcal{V}^\mathrm{I}_\alpha$ from Eq. (58) one needs to differentiate $\mathcal{H}^\mathrm{W}(\mathbf{k})$, which can be easily done with the help of Eq. (69),

$$\partial_\alpha \mathcal{H}^\mathrm{W}_{ij}(\mathbf{k}) = i\sum_\mathbf{R}(R+\tau_j-\tau_i)_\alpha e^{i\mathbf{k}\cdot(\mathbf{R}+\boldsymbol{\tau}_j-\boldsymbol{\tau}_i)}\mathcal{H}_{ij}(\mathbf{R}). \tag{72}$$

In addition, to evaluate $\mathcal{K}^\mathrm{E}_{\alpha\beta}$ from Eq. (60c) one also needs $\mathcal{F}^\mathrm{W}_{\alpha\beta}$. Starting from its definition in Eq. (55) and again using Eq. (69), one finds

$$\mathcal{F}^\mathrm{W}_{\alpha\beta,ij}(\mathbf{k}) = i\sum_\mathbf{R}(R+\tau_j-\tau_i)_\alpha e^{i\mathbf{k}\cdot(\mathbf{R}+\boldsymbol{\tau}_j-\boldsymbol{\tau}_i)}\mathcal{A}_{\beta,ij}(\mathbf{R}) - (\alpha\leftrightarrow\beta). \tag{73}$$

Once all the necessary ingredients are assembled, $\sigma_{\alpha\beta\gamma}$ is computed using Eq. (13).

The way we have presented the interpolation of orbital matrices follows Ref. [24], except for the inclusion of the Wannier centers in the Fourier phase factors. In this formulation, the real-space orbital matrices contain, in each factor depending on $\mathbf{r}$, the position of only one of the two Wannier centers involved, either $\boldsymbol{\tau}_i$ or $\mathbf{R}+\boldsymbol{\tau}_j$: see Eq. (71).

Recently, an improved procedure was introduced [42], whereby the Wannier centers $\boldsymbol{\tau}_i$ and $\mathbf{R}+\boldsymbol{\tau}_j$ are replaced by their average $(\mathbf{R}+\boldsymbol{\tau}_i+\boldsymbol{\tau}_j)/2$. This formulation preserves symmetries better, has a faster convergence with respect to the size of the coarse $\mathbf{q}$ grid, and preserves the generalized Hermiticity conditions in Eqs. (21) and (54), which in the standard approach [24] are only satisfied in the limit of a dense $\mathbf{q}$ grid. Our implementation uses this revised procedure, which we discuss in Appendix C for completeness.

V. RESULTS

In this section we present our results for the optical activity of selected materials, and compare with previous works. The workflow is summarized in Fig. 3, and a more complete schematic is provided in the Supplemental Material [43].

We start with an *ab initio* ground-state calculation performed using QUANTUM ESPRESSO, which provides the Kohn-Sham Bloch eigenstates and energy eigenvalues on the coarse $\mathbf{q}$ mesh. This is followed by the wannierization of the low-energy *ab initio* electronic structure. In this step, the *ab initio* matrices listed in Table I are computed with PW2WANNIER90, and the wannierization matrices $\tilde{W}(\mathbf{q})$ in Eq. (39) are subsequently generated by WANNIER90. The final step—the Wannier interpolation of $\sigma_{\alpha\beta\gamma}(\omega)$—is carried out using the WANNIERBERRI code [37], where the methodology presented in this work was implemented.

All the materials studied are either semiconductors or insulators, thus only the Fermi-sea terms in Eq. (13) and in Fig. 1

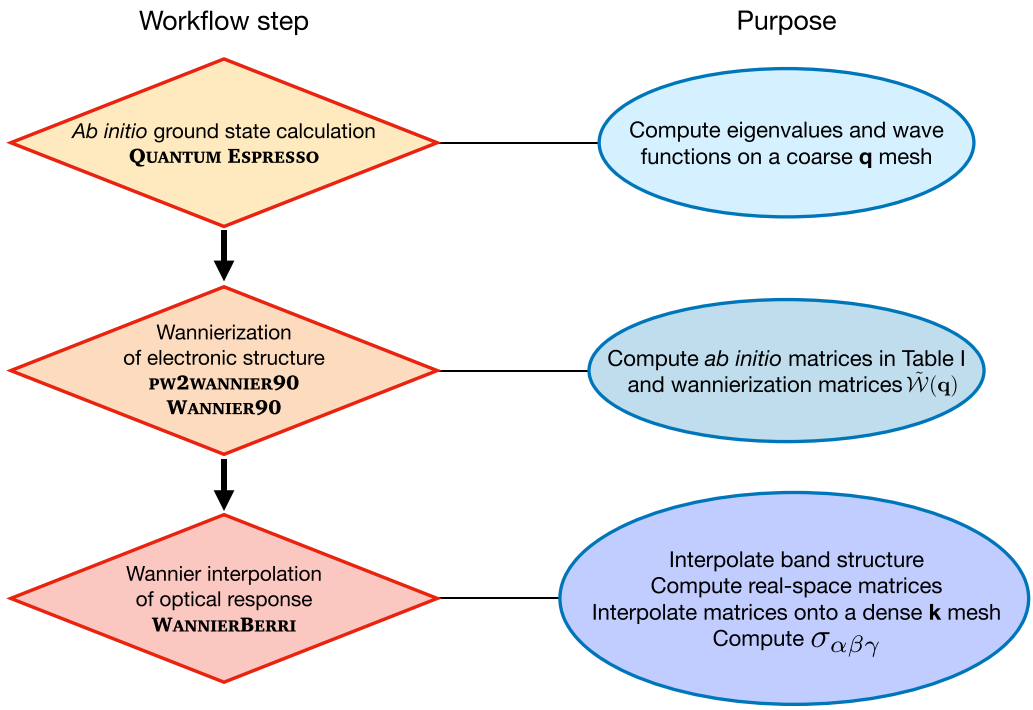

FIG. 3. Workflow of the computational approach used for evaluating the spatially dispersive optical conductivity.

contribute at zero electronic temperature. Moreover, since all the materials studied are nonmagnetic, the spin contribution to $\sigma_{\alpha\beta\gamma}$ vanishes in the absence of SOC. With SOC, the spin terms are found to be negligible.

A. Computational details

1. Density-functional theory calculations

Density-functional theory (DFT) electronic-structure calculations are performed for wurtzite GaN, trigonal Se and Te, and α-SiO_2 using QUANTUM ESPRESSO. The local density approximation (LDA) is employed for GaN, and the generalized gradient approximation (GGA) for Se and α-SiO_2. LDA calculations use the Perdew-Zunger [44] parametrization of the exchange-correlation energy, while GGA calculations use the Perdew-Burke-Ernzerhof (PBE) functional [45]. In the case of Te, exact Fock exchange is added on top of the PBE exchange-correlation energy, adopting a Heyd-Scuseria-Ernzerhof [46] hybrid functional.

The ions are described via scalar-relativistic and fully-relativistic optimized norm-conserving Vanderbilt pseudopotentials [47]. Specifically, for GaN, Se, and α-SiO_2 we use scalar-relativistic pseudopotentials (valence configurations: $3d^{10}4s^24p^1$ for Ga, $2s^22p^3$ for N, $3d^{10}4s^24p^4$ for Se, $3s^23p^2$ for Si, and $2s^22p^4$ for O), whereas for Te we use both scalar-relativistic and full-relativistic pseudopotentials (valence configuration $4d^{10}5s^25p^4$). The pseudo-wavefunctions are expanded in plane-wave basis sets with kinetic energy cut-offs of 80 Ry for GaN, 60 Ry for Te, and 100 Ry for both Se and α-SiO_2.

The BZ is sampled using Γ-centered Monkhorst-Pack meshes [48]. The mesh size is $6 \times 6 \times 4$ for GaN, $6 \times 6 \times 6$ for Te and α-SiO_2, and $8 \times 8 \times 8$ for Se.

2. Construction of Wannier functions

For the construction of Wannier functions using WANNIER90, we choose atom-centered s and p trial orbitals for each atomic species in each material studied; the one exception is oxygen in α-SiO_2, for which we use p orbitals only. These choices correspond to the dominant orbital character of the highest occupied and lowest unoccupied bands. The disentanglement procedure [34] is used when necessary. Details about the ranges of the frozen and disentanglement energy windows adopted for each material are provided in the Supplemental Material [43].

The resulting Wannier functions reproduce the low-energy *ab initio* electronic structure around the Fermi level. As discussed in Sec. IV B 1, this allows us to compute the absorptive part of the low-frequency optical conductivity $\sigma_{\alpha\beta\gamma}(\omega)$ without any band-truncation errors. On the other hand, the reactive part of the calculated optical response does suffer from these errors.

The Wannier functions generated by WANNIER90 slightly break crystal symmetries, because symmetry is not enforced in the wannierization algorithm. To ensure that the calculated $\sigma_{\alpha\beta\gamma}$ tensor complies with the point-group symmetry, two seperate symmetrization procedures are applied during Wannier interpolation, as described in Appendix D 1.

When studying in Appendix D 2 the effect of band-truncation errors on the rotatory power of Se, we need to wannierize a number of empty states that is larger than those accessible by using only s and p trial orbitals. To that end, we exploit the "selected columns of the density matrix" (SCDM) method [49,50], as implemented in WANNIER90 [51]. This method is used as a guide to identify the centers of the Wannier functions that span the additional conduction bands. We interpret those Wannier functions as interstitial orbitals,

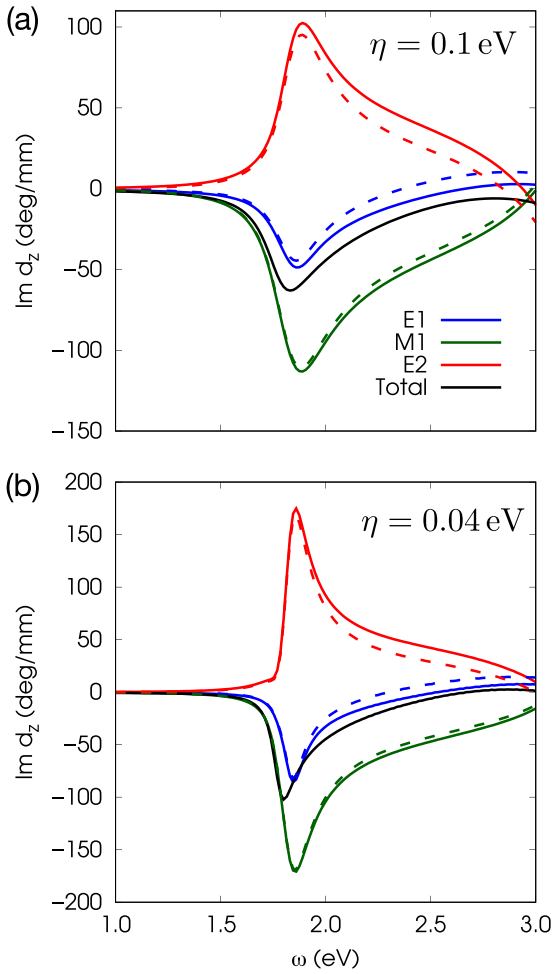

FIG. 4. Absorptive part of the polar optical activity spectrum of GaN, calculated with two different broadening parameters η and broken down into E1, M1, and E2 contributions. Dashed lines indicate the decomposition used in Ref. [20] (where the E1 terms were denoted as "band dispersion"), while solid lines indicate the revised decomposition presented in this work.

for which s-like trial orbitals are used. A more detailed explanation is provided in the Supplemental Material [43].

B. Polar optical activity of wurtzite GaN

Wurtzite is a polar structure with point group $6mm$, whose gyration tensor is purely antisymmetric and therefore shows neither optical rotation nor circular dichroism (Sec. II A). With the polar axis along z, the nonzero tensor components are $G_{xy} = -G_{yx} (= G_z)$, which map onto d_z via Eq. (8). We evaluate as a function of frequency its absorptive (imaginary) part, and compare it with a recent Kubo-formula calculation [20] that used a sum-over-states approach (Sec. III).

Figure 4 shows the calculated spectrum from 1 to 3 eV (solid black line), broken down into E1, M1, and E2 terms (solid colored lines). This decomposition, depicted schematically in Fig. 1 and detailed in Appendix A, is somewhat different from that in Ref. [20], which is also shown in Fig. 4 as calculated in the present work (dashed lines). The spectrum in Fig. 4(a) is obtained using an interpolation mesh of $198 \times 198 \times 132$ **k** points. Since the details of the spectrum at frequencies near the band gap are particularly sensitive to the broadening parameter η, we adopt $\eta = 0.1$ eV as in Ref. [20] for a better comparison. Both the relative peak positions and their heights are in good quantitative agreement with that work, as shown in Fig. S5 within the Supplemental Material [43]. The main differences arise in the E1 contribution at frequencies above the band gap, which could possibly be caused by the band truncation error inherent to the method used in Ref. [20], and to the different sampling density of reciprocal space.

The M1 and E2 terms cancel to a large extent in Fig. 4(a), so that $\mathrm{Im}\, d_z(\omega)$ follows closely the E1 term [20]. However, E2 has a sharper rise compared to M1, which makes the cancellation incomplete for frequencies just below the gap, pushing the resonance peak to lower frequencies by about 0.05 eV. This can be better appreciated by reducing the broadening parameter to $\eta = 0.04$ eV and sampling the BZ on a denser $300 \times 300 \times 200$ mesh to ensure convergence. The resulting spectrum in Fig. 4(b) reveals an additional E2 feature close to the band-gap frequency.

C. Rotatory power of tellurium, selenium, and α-quartz

Recently, the rotatory power of several chiral materials was computed using both Kubo [20] and DFPT [22] methods. The latter is at present restricted to the low-frequency limit, but it includes local-field effects that are instead neglected in the former. As mentioned earlier, such effects were found to play a substantial role in the optical rotation of certain materials [22,23].

Here, we compute the rotatory power of trigonal Te, trigonal Se, and α-SiO_2. The results for Te are compared with the Kubo calculations of Ref. [20] and with experimental measurements [27,28]. In the case of Se and α-SiO_2, we compare with the DFPT results of Ref. [22].

All three materials are chiral, with their left- and right-handed enantiomorphs crystallizing in the $P3_221$ and $P3_121$ space groups, respectively (point group 32). The gyration tensor is diagonal, with $G_{xx} = G_{yy} \neq G_{zz}$. According to Eq. (6), the rotatory power for light propagating along the trigonal z axis is given by

$$\rho(\omega) = \frac{\omega^2}{2c^2} \mathrm{Re}\, G_{zz}(\omega). \tag{74}$$

The calculations reported below were carried out for the left-handed enantiomorphs.

1. Tellurium

Figure 5(a) shows the rotatory-power spectrum of tellurium, calculated both with and without SOC using a $200 \times 200 \times 150$ interpolation mesh, together with experimental data from Refs. [27,28]. Due to the large atomic number of Te, SOC plays a substantial role. The spectrum computed without SOC overestimates the experimental one, while that obtained with SOC underestimates it.

The band gap is important in determining $\rho(\omega)$. Since reactive and absorptive responses satisfy Kramers-Krönig relations, $\rho(\omega)$ shows a resonance at the gap frequency where circular dichroism sets in. This, in turn, affects the rate at

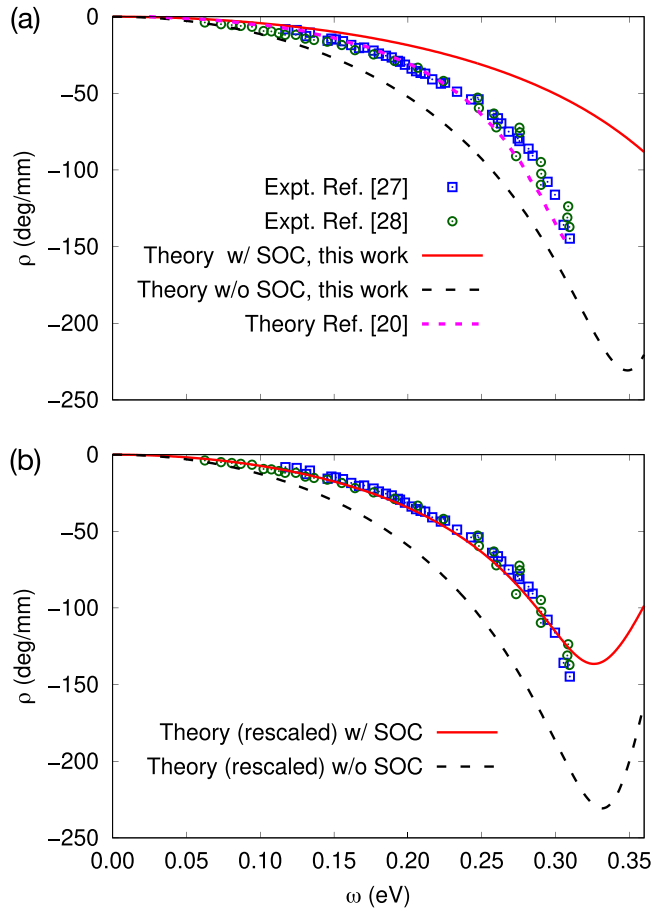

FIG. 5. Calculated and experimental rotatory power of left-handed trigonal Te for light propagating along the trigonal axis. (a) Raw calculated data compared to experimental data [27,28] and to a previous theoretical calculation [20]. For a meaningful comparison with Ref. [20], we use the same broadening parameter, $\eta = 35$ meV, as in that work. (b) Same data as in (a), with a rescaled frequency axis for the theoretical results, to align the *ab initio* energy gap with the experimental one.

which $\rho(\omega)$ increases at subgap frequencies. An accurate band gap is therefore important to obtain a spectrum in good agreement with experiment. For this reason, our calculations were performed with a hybrid functional (see Sec. V A), which typically provides improved band gaps compared to LDA and PBE. This is particularly true for Te, where hybrid-functional calculations with (without) SOC give a band gap of 0.42 eV (0.342 eV), to be compared with the experimental value of 0.323 eV [52]. Instead, the PBE band gap is 0.015 eV [20], 20 times smaller than experiment.

Even though hybrid functionals provide a substantially improved electronic structure, the band gap obtained with SOC is still 0.1 eV larger than experiment. This pushes up the $\rho(\omega)$ resonance resulting in a slower increase at subgap frequencies, which could explain the underestimation of the experimental spectrum. To test this conjecture, in Fig. 5(b) we renormalize the frequency axis to align the resonance frequency with the experimental band gap. This *ad hoc* correction significantly improves the results obtained with SOC.

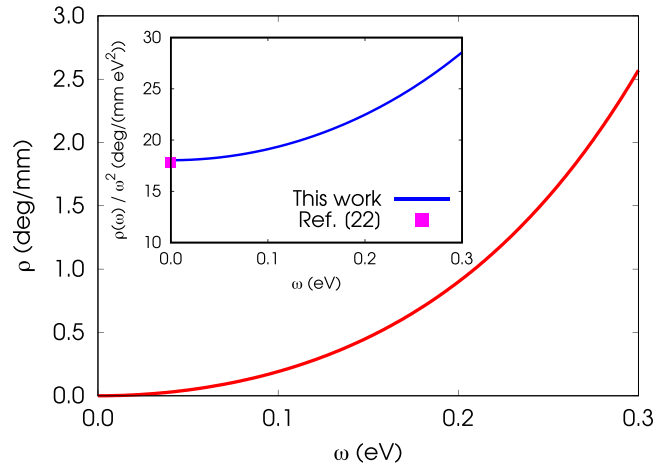

FIG. 6. Calculated rotatory power of trigonal Se for light propagating along the trigonal axis. (Inset) Rotatory power divided by ω^2, which tends to a nonzero constant at low frequencies.

2. *Selenium and α-quartz*

The rotatory power of both elemental Se (isostructural to Te) and α-SiO_2 is strongly affected by local-field effects [22,23]. The $\omega \to 0$ limit of the quantity $\bar{\rho}(\omega) = \rho(\omega)/\omega^2$ introduced in Eq. (7) was computed in Ref. [22] using a DFPT approach. It was found that the removal of local-field effects reduces $\bar{\rho}(0)$ by factors of 4 and 7 for Se and α-SiO_2, respectively.

Figure 6 shows our results for the rotatory power of Se, obtained with a $50 \times 50 \times 36$ interpolation mesh, much coarser than for Te owing to the larger band gap (≈0.96 eV). The quantity $\bar{\rho}(\omega)$ is plotted in the inset, and its value at $\omega = 0$ is in agreement with that obtained in Ref. [22] without self-consistent fields, see Table II [53]. To calculate the rotatory power of α-SiO_2, we use a $100 \times 100 \times 100$ interpolation grid. Also in this case, the value of $\bar{\rho}(0)$ is in reasonable agreement with the one obtained in Ref. [22] without self-consistent terms.

Since optical rotation is a reactive response, its calculation with our methodology is affected by band-truncation errors (see Sec. IV B 1). It is therefore important to assess the convergence of $\rho(\omega)$ with respect to the number of conduction bands spanned by the Wannier basis. In Appendix D 2 we present such a convergence test for Se.

VI. SUMMARY AND OUTLOOK

Wannier interpolation is a fast and accurate technique for computing **k**-dependent quantities across the BZ, using Wannier functions as a tight-binding-like representation of

TABLE II. Static limit of $\bar{\rho}(\omega) = \rho(\omega)/\omega^2$ in comparison with the results of Ref. [22] without and with local fields (LF).

	This work	Ref. [22] w/o LF	Ref. [22] w/LF
Se	18.0	17.8	74.5
α-SiO_2	−1.1	−0.7	−4.9

the low-energy *ab initio* electronic structure. The method is widely used to evaluate the k-space Berry curvature and its BZ integral—the intrinsic anomalous Hall conductivity [24]. Other applications include computing $\sigma_{\alpha\beta}(\omega)$ (the optical conductivity in the E1 approximation) [25,54], and the ground-state orbital magnetization [26,55]. For a comprehensive review, see Ref. [56].

In this work, we developed and implemented a Wannier interpolation scheme to evaluate the Kubo-Greenwood formula (13) for $\sigma_{\alpha\beta\gamma}(\omega)$, the optical conductivity of bulk crystals at first order in the wavevector of light. This quantity contains not only E1 matrix elements as in the case of the Berry curvature and $\sigma_{\alpha\beta}(\omega)$, but also M1 and E2 matrix elements. The latter are trickier to evaluate, as they involve virtual interband transitions; by expressing them as k derivatives, the intermediate band summations were circumvented, avoiding a source of truncation errors that was present in a prior *ab initio* implementation [20].

The proposed method is particularly well suited to compute the absorptive part of $\sigma_{\alpha\beta\gamma}(\omega)$ (e.g., circular dichroism) in the energy range covered by the Wannier basis, which is done without introducing any band-truncation errors. On the other hand, such errors do occur for the reactive response (e.g., rotatory power), which is effectively evaluated as a truncated Kramers-Krönig transform of the absorptive response. Methods based on DFPT [22] seem better suited to obtain the reactive response with high accuracy, as they completely avoid band summations and explicitly account for local-field effects. Nevertheless, our tests indicate that the proposed method can give semiquantitative results for the rotatory power with a manageable number of Wannier functions.

The method was applied to the optical activity of insulators and semiconductors at zero temperature, for which the Fermi-surface terms in Eq. (13)—both intraband and interband—do not play any role. In metals and doped semiconductors such terms do contribute to the optical activity, yielding in the static limit the kinetic magnetoelectric effect (the bulk version of the Edelstein effect at surfaces) [21]. The low-frequency optical activity of conductors arising from these terms is an interesting topic for future studies employing the present method. Another promising direction is to consider the time-odd (symmetric) part of $\sigma_{\alpha\beta\gamma}(\omega)$; that part becomes nonzero in acentric antiferromagnetic materials, giving rise to characteristic optical and static responses.

ACKNOWLEDGMENTS

The authors thank Massimiliano Stengel, Seung-Ju Hong, and Cheol-Hwan Park for valuable discussions, and Xiaoming Wang for sharing computational data relative to Ref. [20]. This work has been supported by the NSF Grant No. DMR-2421895. A.U. acknowledges support from the Abrahams Postdoctoral Fellowship of the Center for Materials Theory at Rutgers University. I.S., O.P.O., and S.S.T. acknowledge support from Grant No. PID2021-129035NB-I00 funded by MCIN/AEI/10.13039/501100011033 and by ERDF/EU, and from the IKUR Strategy under the collaboration agreement between the Ikerbasque Foundation and the Material Physics Center on behalf of the Department of Universities, Science and Innovation of the Basque Government. S.S.T. acknowledges support from the European Union [H2020-MSCA-COFUND-2020-101034228-WOLFRAM2]. Computational resources were provided by the Beowulf cluster at the Department of Physics and Astronomy at Rutgers University.

DATA AVAILABILITY

The data that support the findings of this article are openly available [57].

APPENDIX A: MULTIPOLE-LIKE EXPANSION OF THE OPTICAL MATRIX ELEMENTS IN CRYSTALS

In this Appendix we expand to first order in $\mathbf{q}$ the combination of optical matrix elements entering the Kubo formula for the optical conductivity $\sigma_{\alpha\beta}(\omega, \mathbf{q})$, and express the result in a multipole-like form. We leave out spin terms that are straightforward, and focus on the more subtle orbital terms.

1. Finite systems

Before considering bulk crystals, let us work out the standard multipole expansion for finite systems. We start from the paramagnetic current operator written in Fourier space, and expand it to first order in $\mathbf{q}$,

$$J_\alpha(\mathbf{q}) = -\frac{|e|}{2}\left(v_\alpha e^{-i\mathbf{q}\cdot\mathbf{r}} + e^{-i\mathbf{q}\cdot\mathbf{r}} v_\alpha\right) \simeq -|e| v_\alpha + \frac{i|e|}{2} q_\beta (v_\alpha r_\beta + r_\beta v_\alpha). \tag{A1}$$

Next, we take its matrix elements in the eigenstate basis,

$$\begin{aligned}\langle l|J_\alpha(\mathbf{q})|n\rangle \simeq& -|e|\langle l|v_\alpha|n\rangle + \frac{i|e|}{2} q_\beta \sum_p \left(\langle l|v_\alpha|p\rangle\langle p|r_\beta|n\rangle\right. \\ &\left. + \langle l|r_\beta|p\rangle\langle p|v_\alpha|n\rangle\right) \\ =& \, i|e|\omega_{nl}\langle l|r_\alpha|n\rangle + \frac{|e|}{2} q_\beta \\ &\times \sum_p \left(\omega_{pl}\langle l|r_\alpha|p\rangle\langle p|r_\beta|n\rangle\right. \\ &\left. + \omega_{np}\langle l|r_\beta|p\rangle\langle p|r_\alpha|n\rangle\right),\end{aligned} \tag{A2}$$

where the second equality follows from the relation

$$\mathcal{V}_{\alpha,ln} \equiv \langle l|v_\alpha|n\rangle = i\omega_{ln}\langle l|r_\alpha|n\rangle. \tag{A3}$$

Writing the antisymmetric part of the $\mathbf{q}$-linear term according to the first line of Eq. (A2) and the symmetric part according to the second, one finds

$$\langle l|J_\alpha(\mathbf{q})|n\rangle \simeq -i\omega_{nl} d_{\alpha,ln} + i\left(m_{\alpha\beta,ln} + \frac{i}{2}\omega_{nl} q_{\alpha\beta,ln}\right) q_\beta, \tag{A4}$$

where

$$d_{\alpha,ln} = -|e|\langle l|r_\alpha|n\rangle, \tag{A5}$$

$$m_{\alpha\beta,ln} = -\frac{|e|}{2}\langle l|r_\alpha v_\beta - r_\beta v_\alpha|n\rangle, \tag{A6}$$

$$q_{\alpha\beta,ln} = -|e|\langle l|r_\alpha r_\beta|n\rangle \tag{A7}$$

are the E1, M1, and E2 matrix elements, respectively. Equation (A4) is analogous to the Fourier-transformed multipole expansion of a current distribution [5,19,58],

$$J_\alpha(\omega,\mathbf{q}) \simeq -i\omega d_\alpha(\omega) + i\left[m_{\alpha\beta}(\omega) + \frac{i}{2}\omega q_{\alpha\beta}(\omega)\right]q_\beta. \quad \text{(A8)}$$

The matrix elements of the current operator enter the Kubo formula in the combination

$$\langle n|J_\alpha(\mathbf{q})|l\rangle\langle l|J_\beta(-\mathbf{q})|n\rangle, \quad \text{(A9)}$$

which, in view of Eq. (A4), can be written at first order in $\mathbf{q}$ as

$$\langle n|J_\alpha(\mathbf{q})|l\rangle\langle l|J_\beta(-\mathbf{q})|n\rangle \simeq e^2\mathcal{V}_{\alpha,nl}\mathcal{V}_{\beta,ln} + ie^2(\mathcal{V}_{\alpha,nl}\mathcal{T}_{\beta\gamma,ln} - \mathcal{V}_{\beta,ln}\mathcal{T}_{\alpha\gamma,nl})q_\gamma, \quad \text{(A10)}$$

where the velocity matrix $\mathcal{V}_\alpha$ is related to the E1 matrix by Eq. (A3), and the antisymmetric and symmetric parts of $\mathcal{T}_{\alpha\beta}$ give the M1 and E2 matrices, respectively. All in all, we have

$$\omega_{ln}d_{\alpha,ln} = i|e|\mathcal{V}_{\alpha,ln}, \quad \text{(A11a)}$$

$$m_{\alpha\beta,ln} = \frac{|e|}{2}(\mathcal{T}_{\alpha\beta,ln} - \mathcal{T}_{\beta\alpha,ln}), \quad \text{(A11b)}$$

$$\omega_{ln}q_{\alpha\beta,ln} = i|e|(\mathcal{T}_{\alpha\beta,ln} + \mathcal{T}_{\beta\alpha,ln}). \quad \text{(A11c)}$$

2. Bulk crystals

When the expansion (A10) is carried out in the Bloch eigenstate basis, one faces the problem that $\mathbf{k}$ derivatives of cell-periodic Bloch states do not transform covariantly under gauge transformations. By introducing covariant derivatives each term in the expansion becomes gauge covariant [21], and one finds that the matrix $\mathcal{T}_{\alpha\beta}$ appearing in Eq. (A10) is given by Eq. (17) [59]. Using Eq. (18) for $\mathcal{K}_{\alpha\beta}$ and comparing with Eqs. (32) and (A11) leads to

$$\mathfrak{d}_{\alpha,ln} = -i|e|\langle u_l|D_\alpha u_n\rangle = -|e|A_{\alpha,ln}, \quad \text{(A12)}$$

$$\mathfrak{m}_{\alpha\beta,ln} = \frac{|e|}{2i\hbar}\langle D_\alpha u_l|H - \bar{\epsilon}_{ln}|D_\beta u_n\rangle + \frac{|e|}{2}\bar{v}_{\alpha,ln}A_{\beta,ln} - (\alpha\leftrightarrow\beta), \quad \text{(A13)}$$

$$\omega_{ln}\mathfrak{q}_{\alpha\beta,ln} = -\frac{|e|}{2}\omega_{ln}\langle D_\alpha u_l|D_\beta u_n\rangle + i|e|\bar{v}_{\alpha,ln}A_{\beta,ln} + (\alpha\leftrightarrow\beta), \quad \text{(A14)}$$

with $\bar{\epsilon}_{ln} = (\epsilon_l + \epsilon_n)/2$ and $\bar{v}_{\alpha,ln}$ given by Eq. (14e). We denote these multipole-like bulk tensors as $\mathfrak{d}$, $\mathfrak{m}$, and $\mathfrak{q}$ to distinguish them from the standard multipoles d, m, and q in Eqs. (A5)–(A7), which become ill-defined for extended systems.

The expressions above for $\mathfrak{m}_{\alpha\beta}$ and $\mathfrak{q}_{\alpha\beta}$ differ from the ones in Ref. [21] by the presence of the off-diagonal $\bar{v}_\alpha A_\beta$ terms. If Eq. (33) is used for $\mathcal{K}_{\alpha\beta}$ instead of Eq. (18), the following sum-over-states formulas are obtained:

$$\mathfrak{m}_{\alpha\beta,ln} = \frac{i|e|}{4}\sum_{p\neq l}\frac{\mathcal{V}_{\alpha,lp}\mathcal{V}_{\beta,pn} - (\alpha\leftrightarrow\beta)}{\omega_{lp}} - \frac{i|e|}{4}\sum_{p\neq n}\frac{\mathcal{V}_{\alpha,lp}\mathcal{V}_{\beta,pn} - (\alpha\leftrightarrow\beta)}{\omega_{pn}} \quad \text{(A15)}$$

and

$$\omega_{ln}\mathfrak{q}_{\alpha\beta,ln} = \frac{|e|}{2}\sum_{p\neq l}\frac{\mathcal{V}_{\alpha,lp}\mathcal{V}_{\beta,pn} + (\alpha\leftrightarrow\beta)}{\omega_{lp}} + \frac{|e|}{2}\sum_{p\neq n}\frac{\mathcal{V}_{\alpha,lp}\mathcal{V}_{\beta,pn} + \alpha\leftrightarrow\beta)}{\omega_{pn}}. \quad \text{(A16)}$$

In both equations, only the terms with vanishing denominators are excluded. Instead, in the sum-over-state formulas of Ref. [21] an additional nonsingular term is excluded from each summation when $l \neq n$ [60].

Interband orbital moments are needed to evaluate the orbital Hall conductivity, and the expression used in the recent literature [61,62] agrees with the sum-over-states formula of Ref. [21]. The impact on the orbital Hall conductivity of the additional off-diagonal term in Eqs. (A13) and (A15) remains to be studied. As it contains the band velocity, that term is "itinerant" (it vanishes for crystals composed of nonoverlapping units); its contribution should therefore be enhanced in crystals with strongly dispersive bands.

In closing, we note that a different expression for the interband orbital moment has been proposed within the semiclassical wavepacket formalism [63]. That expression is non-Hermitian, and its Hermitian part almost agrees with Eq. (A13), the only difference being that the itinerant $\bar{v}_\alpha A_\beta$ term is twice as large. Upon integrating over the BZ and performing an integration by parts, that term becomes an interband version of the Berry-curvature contribution to the ground-state orbital magnetization of a non-Chern insulator, which reads [64]

$$M_{\alpha\beta} = \sum_n^{\text{occ}}\int[d\mathbf{k}]\left(\mathfrak{m}_{\alpha\beta,nn} - \frac{|e|}{\hbar}\epsilon_n\mathcal{F}_{\alpha\beta,nn}\right), \quad \text{(A17)}$$

with $\mathcal{F}_{\alpha\beta}$ given by Eq. (27) and $\mathfrak{m}_{\alpha\beta}$ by Eq. (A13) ($\mathcal{F}_{\alpha\beta,nn}$ and $\mathfrak{m}_{\alpha\beta,nn}$ are the Berry curvature and the intrinsic orbital moment of a Bloch state, respectively).

APPENDIX B: DERIVATION OF Eq. (60) FOR $\mathcal{K}^{\mathrm{H}}_{\alpha\beta}$

We want to evaluate by Wannier interpolation the matrix $\mathcal{K}_{\alpha\beta}$ defined by Eq. (18). Denoting its first term as $(1/i\hbar)Z_{\alpha\beta}$ and expanding the covariant derivatives according to Eq. (51), we find

$$\begin{aligned} Z^{\mathrm{H}}_{\alpha\beta,ln} = {} & \sum_{i,j}\mathcal{U}^\dagger_{li}\langle\partial_\alpha u^{\mathrm{W}}_i|H-\epsilon_l|\partial_\beta u^{\mathrm{W}}_j\rangle\mathcal{U}_{jn} + i\sum_i\mathcal{U}^\dagger_{li}\langle\partial_\alpha u^{\mathrm{W}}_i|H-\epsilon_l|u^{\mathrm{W}}_n\rangle a^{\mathrm{E}}_{\beta,n} \\ & - i\sum_{p,j}\mathcal{U}^\dagger_{lj}\langle\partial_\alpha u^{\mathrm{W}}_j|H-\epsilon_l|u^{\mathrm{H}}_p\rangle A^{\mathrm{I}}_{\beta,pn} - i\sum_j a^{\mathrm{E}}_{\alpha,l}\langle u^{\mathrm{H}}_l|H-\epsilon_l|\partial_\beta u^{\mathrm{W}}_j\rangle\mathcal{U}_{jn} \\ & + i\sum_{p,j}A^{\mathrm{I}}_{\alpha,lp}\langle u^{\mathrm{H}}_p|H-\epsilon_l|\partial_\beta u^{\mathrm{W}}_j\rangle\mathcal{U}_{jn} + (\epsilon_l-\epsilon_n)A^{\mathrm{I}}_{\alpha,ln}a^{\mathrm{E}}_{\beta,n} + \sum_p(\epsilon_p-\epsilon_l)A^{\mathrm{I}}_{\alpha,lp}A^{\mathrm{I}}_{\beta,pn}, \end{aligned} \quad \text{(B1)}$$

where Eq. (44) was used to eliminate two terms and to simplify two other terms.

Next, use Eq. (43) for the Hamiltonian-gauge Bloch states together with the definitions in Eq. (53) and with the prescription (50) for obtaining external objects. Equation (B1) then becomes

$$\begin{aligned} Z^{\mathrm{H}}_{\alpha\beta,ln} &= \mathcal{D}^{\mathrm{E}}_{\alpha\beta,ln} - \epsilon_l \mathcal{C}^{\mathrm{E}}_{\alpha\beta,ln} - \big[\big(\mathcal{B}^{\mathrm{E}}_{\alpha,nl}\big)^* - \epsilon_l \mathcal{A}^{\mathrm{E}}_{\alpha,ln}\big] a^{\mathrm{E}}_{\beta,n} \\ &\quad + \sum_p \big[\big(\mathcal{B}^{\mathrm{E}}_{\alpha,pl}\big)^* - \epsilon_l \mathcal{A}^{\mathrm{E}}_{\alpha,lp}\big] A^{\mathrm{I}}_{\beta,pn} \\ &\quad - a^{\mathrm{E}}_{\alpha,l}\big(\mathcal{B}^{\mathrm{E}}_{\beta,ln} - \epsilon_l \mathcal{A}^{\mathrm{E}}_{\beta,ln}\big) \\ &\quad + \sum_p A^{\mathrm{I}}_{\alpha,lp}\big(\mathcal{B}^{\mathrm{E}}_{\beta,pn} - \epsilon_l \mathcal{A}^{\mathrm{E}}_{\beta,pn}\big) + (\epsilon_l - \epsilon_n) A^{\mathrm{I}}_{\alpha,ln} a^{\mathrm{E}}_{\beta,n} \\ &\quad + \sum_p (\epsilon_p - \epsilon_l) A^{\mathrm{I}}_{\alpha,lp} A^{\mathrm{I}}_{\beta,pn}. \end{aligned} \tag{B2}$$

To proceed further, assume that both ϵ_l and ϵ_n—but not necessarily ϵ_p—lie inside the frozen window, and use

$$\mathcal{B}^{\mathrm{E}}_{\alpha,np} = \epsilon_n \mathcal{A}^{\mathrm{E}}_{\alpha,np}, \ \forall p \text{ and } \epsilon_n \in \text{ frozen window}. \tag{B3}$$

This relation, which follows from $H|u^{\mathrm{H}}_n\rangle = \epsilon_n |u^{\mathrm{H}}_n\rangle$, holds exactly when the interpolation point $\mathbf{k}$ falls on the *ab initio* mesh ($\mathbf{k} = \mathbf{q}$), and it holds to an excellent approximation otherwise; when ϵ_n lies outside the frozen window $|u^{\mathrm{H}}_n\rangle$ ceases to be an eigenstate of H, and as a result Eq. (B3) does not hold even approximately.

Under the stated assumption, Eq. (B3) can be used in the first and third lines of Eq. (B2); it makes the third line vanish, and it turns the quantity inside square brackets in the first line into $(\epsilon_n - \epsilon_l) A^{\mathrm{E}}_{\alpha,ln}$, with A^{E}_{α} the off-diagonal part of $\mathcal{A}^{\mathrm{E}}_{\alpha}$. Separating $Z^{\mathrm{H}}_{\alpha\beta}$ into internal, external and cross terms we find

$$Z^{\mathrm{I}}_{\alpha\beta,ln} = \sum_p (\epsilon_p - \epsilon_l) A^{\mathrm{I}}_{\alpha,lp} A^{\mathrm{I}}_{\beta,pn}, \tag{B4}$$

$$Z^{\mathrm{E}}_{\alpha\beta,ln} = \mathcal{D}^{\mathrm{E}}_{\alpha\beta,ln} - \epsilon_l \mathcal{C}^{\mathrm{E}}_{\alpha\beta,ln} + (\epsilon_l - \epsilon_n) A^{\mathrm{E}}_{\alpha,ln} a^{\mathrm{E}}_{\beta,n}, \tag{B5}$$

$$\begin{aligned} Z^{\mathrm{X}}_{\alpha\beta,ln} &= \sum_p A^{\mathrm{I}}_{\alpha,lp}\big(\mathcal{B}^{\mathrm{E}}_{\beta,pn} - \epsilon_l \mathcal{A}^{\mathrm{E}}_{\beta,pn}\big) + \sum_p \big[\big(\mathcal{B}^{\mathrm{E}}_{\alpha,pl}\big)^* \\ &\quad - \epsilon_l \mathcal{A}^{\mathrm{E}}_{\alpha,lp}\big] A^{\mathrm{I}}_{\beta,pn} + (\epsilon_l - \epsilon_n) A^{\mathrm{I}}_{\alpha,ln} a^{\mathrm{E}}_{\beta,n}. \end{aligned} \tag{B6}$$

The matrix $\mathcal{K}^{\mathrm{H}}_{\alpha\beta}$ defined by Eq. (18) can be similarly decomposed. The internal part of its first term is given by Eq. (B4) divided by $i\hbar$, and to evaluate its second term we use Eqs. (57) and (59) for the interband Berry connection and for the band velocity, respectively. Collecting all internal terms we obtain [compare with Eq. (36)]

$$\begin{aligned} \mathcal{K}^{\mathrm{I}}_{\alpha\beta,ln} &= \frac{1}{i\hbar} \sum_p (\epsilon_p - \epsilon_l) A^{\mathrm{I}}_{\alpha,lp} A^{\mathrm{I}}_{\beta,pn} + \mathcal{V}^{\mathrm{I}}_{\alpha,ll} A^{\mathrm{I}}_{\beta,ln} \\ &= \sum_{p \neq l} \mathcal{V}^{\mathrm{I}}_{\alpha,lp} A^{\mathrm{I}}_{\beta,pn} + \mathcal{V}^{\mathrm{I}}_{\alpha,ll} A^{\mathrm{I}}_{\beta,ln} \\ &= \sum_p \mathcal{V}^{\mathrm{I}}_{\alpha,lp} A^{\mathrm{I}}_{\beta,pn}, \end{aligned} \tag{B7}$$

which corresponds to Eq. (60b).

To evaluate the external part of $\mathcal{K}^{\mathrm{H}}_{\alpha\beta}$, use Eqs. (B5) and (57) in Eq. (18); after converting band energies and band velocities to matrix form, we obtain Eq. (60c).

Finally, to evaluate the cross term $\mathcal{K}^{\mathrm{X}}_{\alpha\beta} = (1/i\hbar) Z^{\mathrm{X}}_{\alpha\beta}$, split $\mathcal{A}^{\mathrm{E}}_{\beta}$ and $\mathcal{B}^{\mathrm{E}}_{\beta}$ into interband and intraband parts as

$$\mathcal{A}^{\mathrm{E}}_{\beta,pn} = A^{\mathrm{E}}_{\beta,pn} + \delta_{pn} a^{\mathrm{E}}_{\beta,n}, \tag{B8}$$

$$\mathcal{B}^{\mathrm{E}}_{\beta,pn} = B^{\mathrm{E}}_{\beta,pn} + \delta_{pn} \epsilon_n a^{\mathrm{E}}_{\beta,n} \tag{B9}$$

(the second relation is only valid for ϵ_n inside the frozen window). Inserting these expressions in Eq. (B6) gives

$$\begin{aligned} Z^{\mathrm{X}}_{\alpha\beta,ln} &= \sum_p A^{\mathrm{I}}_{\alpha,lp}\big(B^{\mathrm{E}}_{\beta,pn} - \epsilon_l A^{\mathrm{E}}_{\beta,pn}\big) \\ &\quad + \sum_p \big[\big(B^{\mathrm{E}}_{\alpha,pl}\big)^* - \epsilon_l A^{\mathrm{E}}_{\alpha,lp}\big] A^{\mathrm{I}}_{\beta,pn} \\ &\quad + \epsilon_n A^{\mathrm{I}}_{\alpha,ln} a^{\mathrm{E}}_{\beta,n} - \epsilon_l A^{\mathrm{I}}_{\alpha,ln} a^{\mathrm{E}}_{\beta,n} + \epsilon_l a^{\mathrm{E}}_{\alpha,l} A^{\mathrm{I}}_{\beta,ln} \\ &\quad - \epsilon_l a^{\mathrm{E}}_{\alpha,l} A^{\mathrm{I}}_{\beta,ln} + (\epsilon_l - \epsilon_n) A^{\mathrm{I}}_{\alpha,ln} a^{\mathrm{E}}_{\beta,n}. \end{aligned} \tag{B10}$$

The terms in the third and fourth line cancel out, and dividing the first two lines by $i\hbar$ we arrive at Eq. (60d).

APPENDIX C: IMPROVED SCHEME FOR EVALUATING THE REAL-SPACE ORBITAL MATRICES

Here, we describe the improved procedure to evaluate the real-space matrices [42], mentioned in Sec. IV B 3, that is used in our implementation. The idea is to introduce recentered real-space matrices where the Wannier centers $\boldsymbol{\tau}_i$ and $\mathbf{R} + \boldsymbol{\tau}_j$ in Eq. (71) are both replaced by their average

$$\bar{\mathbf{r}}_{ij}(\mathbf{R}) = \tfrac{1}{2}(\mathbf{R} + \boldsymbol{\tau}_j + \boldsymbol{\tau}_i), \tag{C1}$$

resulting in

$$\bar{\mathcal{A}}_{\alpha,ij}(\mathbf{R}) = \langle \mathbf{0}i | [r - \bar{r}_{ij}(\mathbf{R})]_\alpha | \mathbf{R}j \rangle, \tag{C2a}$$

$$\bar{\mathcal{B}}_{\alpha,ij}(\mathbf{R}) = \langle \mathbf{0}i | H [r - \bar{r}_{ij}(\mathbf{R})]_\alpha | \mathbf{R}j \rangle, \tag{C2b}$$

$$\bar{\mathcal{C}}_{\alpha\beta,ij}(\mathbf{R}) = \langle \mathbf{0}i | [r - \bar{r}_{ij}(\mathbf{R})]_\alpha [r - \bar{r}_{ij}(\mathbf{R})]_\beta | \mathbf{R}j \rangle, \tag{C2c}$$

$$\bar{\mathcal{D}}_{\alpha\beta,ij}(\mathbf{R}) = \langle \mathbf{0}i | [r - \bar{r}_{ij}(\mathbf{R})]_\alpha H [r - \bar{r}_{ij}(\mathbf{R})]_\beta | \mathbf{R}j \rangle. \tag{C2d}$$

Once these recentered matrices have been computed as described below, the original ones in Eq. (71) are recovered using

$$\mathcal{A}_{\alpha,ij}(\mathbf{R}) = \bar{\mathcal{A}}_{\alpha,ij}(\mathbf{R}), \tag{C3a}$$

$$\mathcal{B}_{\alpha,ij}(\mathbf{R}) = \bar{\mathcal{B}}_{\alpha,ij}(\mathbf{R}) - d_{\alpha,ij}(\mathbf{R}) \mathcal{H}_{ij}(\mathbf{R}), \tag{C3b}$$

$$\begin{aligned} \mathcal{C}_{\alpha\beta,ij}(\mathbf{R}) &= \bar{\mathcal{C}}_{\alpha\beta,ij}(\mathbf{R}) + d_{\alpha,ij}(\mathbf{R}) \bar{\mathcal{A}}_{\beta,ij}(\mathbf{R}) \\ &\quad - d_{\beta,ij}(\mathbf{R}) \bar{\mathcal{A}}_{\alpha,ij}(\mathbf{R}), \end{aligned} \tag{C3c}$$

$$\begin{aligned} \mathcal{D}_{\alpha\beta,ij}(\mathbf{R}) &= \bar{\mathcal{D}}_{\alpha\beta,ij}(\mathbf{R}) + d_{\alpha,ij}(\mathbf{R}) \bar{\mathcal{B}}_{\beta,ij}(\mathbf{R}) \\ &\quad - d_{\beta,ij}(\mathbf{R}) \bar{\mathcal{B}}_{\alpha,ij}(\mathbf{R}) \\ &\quad - d_{\alpha,ij}(\mathbf{R}) d_{\beta,ij}(\mathbf{R}) \mathcal{H}_{ij}(\mathbf{R}), \end{aligned} \tag{C3d}$$

where

$$\mathbf{d}_{ij}(\mathbf{R}) = \tfrac{1}{2}(\mathbf{R} + \boldsymbol{\tau}_j - \boldsymbol{\tau}_i). \tag{C4}$$

Note that the last term in Eq. (C3d) is symmetric in $\alpha\beta$; since only the antisymmetric part of $\mathcal{D}_{\alpha\beta}$ contributes to $\sigma_{\alpha\beta\gamma}$, that term drops out.

The next step is to evaluate the recentered matrices via the approximate identity

$$\mathbf{r} - \mathbf{r}_0 \simeq i \sum_{\mathbf{b}} w_b \mathbf{b} e^{-i\mathbf{b}\cdot(\mathbf{r}-\mathbf{r}_0)}, \tag{C5}$$

which follows from expanding the exponential to first order, and then using the relation $\sum_{\mathbf{b}} w_b b_\alpha b_\beta = \delta_{\alpha\beta}$ [33] (the $\mathbf{b}$ vectors connect neighboring points on the $\mathbf{q}$-grid, and w_b are weight factors). Equation (C5) provides an approximate representation of the position operator on a periodic supercell commensurate with the Wannier functions given by Eq. (37). As that representation is most accurate near $\mathbf{r}_0$ [65], the choice $\mathbf{r}_0 = \bar{\mathbf{r}}_{ij}(\mathbf{R})$ (halfway between the Wannier centers $\langle \mathbf{0}i|\mathbf{r}|\mathbf{0}i\rangle$ and $\langle \mathbf{R}j|\mathbf{r}|\mathbf{R}j\rangle$) is optimal for the purpose of evaluating orbital matrix elements between $|\mathbf{0}i\rangle$ and $|\mathbf{R}j\rangle$.

To proceed, write

$$(\mathbf{r} - \mathbf{r}_0)|\mathbf{R}j\rangle \simeq i \sum_{\mathbf{b}} w_b \mathbf{b} e^{-i\mathbf{b}\cdot(\mathbf{r}-\mathbf{r}_0)}|\mathbf{R}j\rangle, \tag{C6a}$$

$$\langle \mathbf{0}i|(\mathbf{r} - \mathbf{r}_0) \simeq -i \sum_{b} w_b \mathbf{b} \langle \mathbf{0}i|e^{i\mathbf{b}\cdot(\mathbf{r}-\mathbf{r}_0)}, \tag{C6b}$$

plug these expressions into Eq. (C2) setting $\mathbf{r}_0 = \bar{\mathbf{r}}_{ij}(\mathbf{R})$, and then use Eqs. (37) and (38) to express the WFs in terms of the *ab initio* Bloch eigenfunctions. Invoking the orthonormality relation

$$\langle \psi_{\mathbf{q}}|\chi_{\mathbf{q}'}\rangle = N\delta_{\mathbf{q},\mathbf{q}'}\langle u_{\mathbf{q}}|v_{\mathbf{q}}\rangle \tag{C7}$$

between Bloch-like states $\psi_{\mathbf{q}}(\mathbf{r}) = e^{i\mathbf{q}\cdot\mathbf{r}}u_{\mathbf{q}}(\mathbf{r})$ and $\chi_{\mathbf{q}'}(\mathbf{r}) = e^{i\mathbf{q}'\cdot\mathbf{r}}v_{\mathbf{q}'}(\mathbf{r})$, one arrives at

$$\bar{\mathcal{A}}_{\alpha,ij}(\mathbf{R}) \simeq \frac{i}{N}\sum_{\mathbf{b},\mathbf{q}} w_b b_\alpha e^{-i(\mathbf{q}+\mathbf{b}/2)\cdot(\mathbf{R}+\boldsymbol{\tau}_j-\boldsymbol{\tau}_i)} \times [\mathcal{W}^\dagger(\mathbf{q})\mathbb{M}(\mathbf{q},\mathbf{q}+\mathbf{b})\mathcal{W}(\mathbf{q}+\mathbf{b})]_{ij}, \tag{C8a}$$

$$\bar{\mathcal{B}}_{\alpha,ij}(\mathbf{R}) \simeq \frac{i}{N}\sum_{\mathbf{b},\mathbf{q}} w_b b_\alpha e^{-i(\mathbf{q}+\mathbf{b}/2)\cdot(\mathbf{R}+\boldsymbol{\tau}_j-\boldsymbol{\tau}_i)} \times [\mathcal{W}^\dagger(\mathbf{q})\mathbb{H}(\mathbf{q})\mathbb{M}(\mathbf{q},\mathbf{q}+\mathbf{b})\mathcal{W}(\mathbf{q}+\mathbf{b})]_{ij}, \tag{C8b}$$

$$\bar{\mathcal{C}}_{\alpha\beta,ij}(\mathbf{R}) \simeq \frac{1}{N}\sum_{\mathbf{b},\mathbf{b}',\mathbf{q}} w_b w_{b'} b_\alpha b'_\beta e^{-i(\mathbf{q}+\mathbf{b}/2+\mathbf{b}'/2)\cdot(\mathbf{R}+\boldsymbol{\tau}_j-\boldsymbol{\tau}_i)} \times [\mathcal{W}^\dagger(\mathbf{q}+\mathbf{b})\mathbb{M}(\mathbf{q}+\mathbf{b},\mathbf{q}+\mathbf{b}')\mathcal{W}(\mathbf{q}+\mathbf{b}')]_{ij}, \tag{C8c}$$

$$\bar{\mathcal{D}}_{\alpha\beta,ij}(\mathbf{R}) \simeq \frac{1}{N}\sum_{\mathbf{b},\mathbf{b}',\mathbf{q}} w_b w_{b'} b_\alpha b'_\beta e^{-i(\mathbf{q}+\mathbf{b}/2+\mathbf{b}'/2)\cdot(\mathbf{R}+\boldsymbol{\tau}_j-\boldsymbol{\tau}_i)} \times [\mathcal{W}^\dagger(\mathbf{q}+\mathbf{b})\mathbb{N}(\mathbf{q}+\mathbf{b},\mathbf{q}+\mathbf{b}')\mathcal{W}(\mathbf{q}+\mathbf{b}')]_{ij}, \tag{C8d}$$

where $\mathbb{H}$, $\mathbb{M}$, and $\mathbb{N}$ are the *ab initio* matrices introduced in Eq. (67), and $\mathcal{W}$ is the wannierization matrix of Eq. (38).

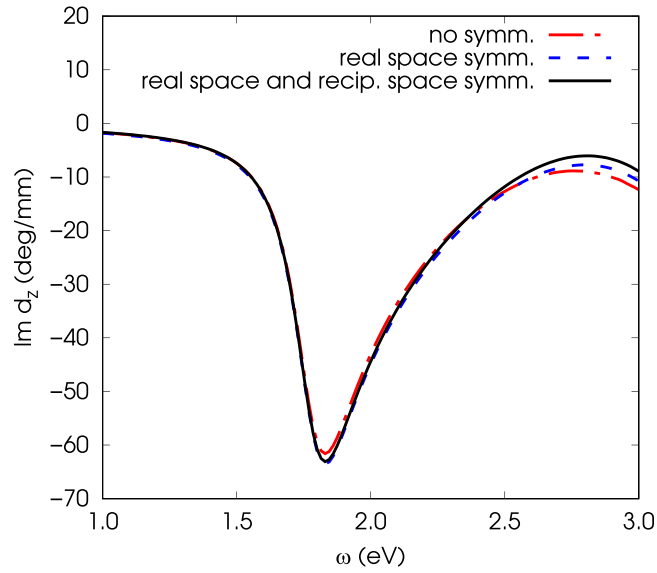

FIG. 7. Absorptive part of the polar optical activity spectrum of GaN obtained with different levels of symmetrization: no symmetrization (red dashed-dotted line), symmetrization of the real-space matrices (blue dashed line), symmetrization both in real space and in reciprocal space (black solid line). The latter is the same as the black solid line in Fig. 4(a).

APPENDIX D: NUMERICAL TESTS

1. Symmetrization

As mentioned in Sec. V A 2, the Wannier functions employed in this work do not fully respect crystal symmetries. Here, we test the two symmetrization procedures that we use to correct for this slight symmetry breaking in the calculation of $\sigma_{\alpha\beta\gamma}(\omega)$. The first is symmetrization of the real-space matrices defined in Sec. IV B, for which we follow the approach first implemented in Ref. [66] for the Hamiltonian matrix, and later generalized to other matrices as well [67]. The second, performed in reciprocal space, uses point-group symmetry to reduce the $\mathbf{k}$ summations to the irreducible wedge of the BZ [37].

To check that the above symmetrization procedures are properly implemented, we calculate in three different ways for GaN the quantity $\mathrm{Im}\, d_z(\omega)$ displayed in Fig. 4: (i) no symmetrization, (ii) symmetrization for the real-space matrix elements but no symmetrization in reciprocal space, and (iii) symmetrization in both real and reciprocal space. The results are shown in Fig. 7. If the Wannier functions respected all point-group symmetries, the three curves would be identical; the small deviations among them suggest that the symmetry breaking is minor.

Symmetry breaking in Wannier interpolation can be avoided altogether by using symmetry-adapted Wannier functions [68]. However, their current implementation in WANNIER90 has two limitations: It does not allow for a frozen window in the disentanglement procedure, and it does not take SOC into account. These limitations prevented us from using symmetry-adapted Wannier functions in the present work [69].

2. Convergence of rotatory power vs wannierized conduction states

As discussed in Sec. IV B 1, in our Wannier interpolation scheme the reactive part of $\sigma_{\alpha\beta\gamma}(\omega)$ is affected by a band-truncation error. To assess its magnitude, here we recalculate the rotatory power of Se using augmented sets of Wannier functions.

The results for Se reported in Sec. V C 2 were obtained with 12 Wannier functions per primitive cell, constructed from atom-centered s and p trial orbitals. This Wannier basis covers the nine valence bands and the three lowest conduction bands. To describe higher conduction bands, we use additional s-like Wannier functions centered at interstitial sites, identified using the SCDM method (see the Supplemental Material [43] for more details). In this way, we are able to describe a total of 18 (9 valence and 9 conduction) and 24 (9 valence and 15 conduction) bands.

In Fig. 8 we display the quantity $\bar{\rho}(\omega) = \rho(\omega)/\omega^2$ defined in Eq. (7), computed using the three Wannier basis sets; the curve corresponding to 12 Wannier functions is the same as in the inset of Fig. 6. The convergence with respect to the number of Wannier functions is somewhat slow and nonmonotonic, with $\bar{\rho}(\omega)$ changing by roughly a factor of two when going from 18 to 24 orbitals.

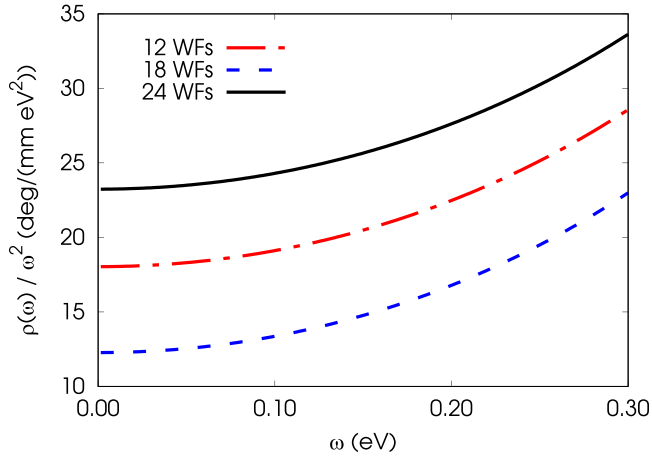

FIG. 8. Dependence on the size of the Wannier-function (WF) basis of the calculated rotatory power of trigonal Se divided by ω^2.

[1] L. D. Landau and E. M. Lifshitz, *Electrodynamics of Continuous Media* (Elsevier, Amsterdam, 1984).

[2] L. D. Barron, *Molecular Light Scattering and Optical Activity* (Cambridge University Press, Cambridge, 2004).

[3] R. E. Newnham, *Properties of Materials* (Oxford University Press, Oxford, 2005).

[4] C. Malgrange, C. Ricolleau, and M. Schlenker, *Symmetry and Physical Properties of Crystals* (Springer, Dordrecht, 2014).

[5] R. E. Raab and O. L. De Lange, *Multipole Theory in Electromagnetism* (Oxford University Press, Oxford, 2005).

[6] J. Brown, W. F. S. Shtrikman, and D. Treves, Possibility of visual observation of antiferromagnetic domains, J. Appl. Phys. **34**, 1233 (1963).

[7] R. M. Hornreich, Gyrotropic birefringence—Phenomenological theory, J. Appl. Phys. **39**, 432 (1968).

[8] R. M. Hornreich and S. Shtrikman, Theory of gyrotropic birefringence, Phys. Rev. **171**, 1065 (1968).

[9] K. Kimura and T. Kimura, Nonvolatile switching of large nonreciprocal optical absorption at shortwave infrared wavelengths, Phys. Rev. Lett. **132**, 036901 (2024).

[10] T. Bondo Pedersen and A. E. Hansen, *Ab initio* calculation and display of the rotatory strength tensor in the random phase approximation. Method and model studies, Chem. Phys. Lett. **246**, 1 (1995).

[11] P. L. Polavarapu, *Ab initio* molecular optical rotations and absolute configurations, Mol. Phys. **91**, 551 (1997).

[12] K. Yabana and G. F. Bertsch, Application of the time-dependent local density approximation to optical activity, Phys. Rev. A **60**, 1271 (1999).

[13] D. Varsano, L. A. Espinosa-Leal, X. Andrade, M. A. L. Marques, R. di Felice, and A. Rubio, Towards a gauge invariant method for molecular chiroptical properties in TDDFT, Phys. Chem. Chem. Phys. **11**, 4481 (2009).

[14] P. L. Polavarapu, Optical rotation: Recent advances in determining the absolute configuration, Chirality **14**, 768 (2002).

[15] J. Autschbach, L. Nitsch-Velasquez, and M. Rudolph, *Time-Dependent Density Functional Response Theory for Electronic Chiroptical Properties of Chiral Molecules* (Springer, Berlin, Germany, 2010).

[16] J. Mattiat and S. Luber, Recent progress in the simulation of chiral systems with real time propagation methods, Helv. Chim. Acta **104**, e2100154 (2021).

[17] K. Natori, Band theory of the optical activity of crystals, J. Phys. Soc. Jpn. **39**, 1013 (1975).

[18] H. Zhong, Z. H. Levine, D. C. Allan, and J. W. Wilkins, Band-theoretic calculations of the optical-activity tensor of α-quartz and trigonal Se, Phys. Rev. B **48**, 1384 (1993).

[19] A. Malashevich and I. Souza, Band theory of spatial dispersion in magnetoelectrics, Phys. Rev. B **82**, 245118 (2010).

[20] X. Wang and Y. Yan, Optical activity of solids from first principles, Phys. Rev. B **107**, 045201 (2023).

[21] O. P. Ocaña and I. Souza, Multipole theory of optical spatial dispersion in crystals, SciPost Phys. **14**, 118 (2023).

[22] A. Zabalo and M. Stengel, Natural optical activity from density-functional perturbation theory, Phys. Rev. Lett. **131**, 086902 (2023).

[23] L. Jönsson, Z. H. Levine, and J. W. Wilkins, Large local-field corrections in optical rotatory power of quartz and selenium, Phys. Rev. Lett. **76**, 1372 (1996).

[24] X. Wang, J. R. Yates, I. Souza, and D. Vanderbilt, *Ab initio* calculation of the anomalous Hall conductivity by Wannier interpolation, Phys. Rev. B **74**, 195118 (2006).

[25] J. R. Yates, X. Wang, D. Vanderbilt, and I. Souza, Spectral and Fermi surface properties from Wannier interpolation, Phys. Rev. B **75**, 195121 (2007).

[26] M. G. Lopez, D. Vanderbilt, T. Thonhauser, and I. Souza, Wannier-based calculation of the orbital magnetization in crystals, Phys. Rev. B **85**, 014435 (2012).

[27] S. Ades and C. H. Champness, Optical activity of tellurium to 20 μm, J. Opt. Soc. Am. **65**, 217 (1975).

[28] S. Fukuda, T. Shiosaki, and A. Kawabata, Infrared optical activity in tellurium, Phys. Status Solidi B **68**, K107 (1975).

[29] J. Jerphagnon and D. S. Chemla, Optical activity of crystals, J. Chem. Phys. **65**, 1522 (1976).

[30] To obtain the dimensionless gyration tensor g as defined in Ref. [1], multiply Eq. (5) by a factor of ω/c. Note also that Eq. (5) differs by a minus sign from the definition in Ref. [29].

[31] P. S. Halasyamani and K. R. Poeppelmeier, Noncentrosymmetric oxides, Chem. Mater. **10**, 2753 (1998).

[32] J. P. Provost and G. Vallee, Riemannian structure on manifolds of quantum states, Commun. Math. Phys. **76**, 289 (1980).

[33] N. Marzari and D. Vanderbilt, Maximally localized generalized Wannier functions for composite energy bands, Phys. Rev. B **56**, 12847 (1997).

[34] I. Souza, N. Marzari, and D. Vanderbilt, Maximally localized Wannier functions for entangled energy bands, Phys. Rev. B **65**, 035109 (2001).

[35] G. Pizzi, V. Vitale, R. Arita, S. Blügel, F. Freimuth, G. Géranton, M. Gibertini, D. Gresch, C. Johnson, T. Koretsune *et al.*, Wannier90 as a community code: New features and applications, J. Phys.: Condens. Matter **32**, 165902 (2020).

[36] More precisely, we use the "minimal-distance replica selection" algorithm described in Refs. [35,37].

[37] S. S. Tsirkin, High performance Wannier interpolation of Berry curvature and related quantities with WannierBerri code, npj Comput. Mater. **7**, 33 (2021).

[38] To avoid the heavy notations $\epsilon^{\mathrm{H}}_{n\mathbf{k}}$, $v^{\mathrm{H}}_{\alpha,n\mathbf{k}}$, and $\omega^{\mathrm{H}}_{ln\mathbf{k}}$, we will denote the interpolated band energies, band velocities and interband frequencies by the same symbols ϵ_n, $v_{\alpha,n}$ and ω_{ln} as their *ab initio* counterparts. When referring to *ab initio* quantities, we will always include the subscript $\mathbf{q}$ for clarity; instead, we will often omit the subscript $\mathbf{k}$ from interpolated quantities.

[39] To avoid discontinuities, our implementation uses a smooth interpolation between evaluating B^{E}_{α} in the two different ways.

[40] P. Giannozzi, S. Baroni, N. Bonini, M. Calandra, R. Car, C. Cavazzoni, D. Ceresoli, G. L. Chiarotti, M. Cococcioni, I. Dabo *et al.*, QUANTUM ESPRESSO: A modular and open-source software project for quantum simulations of materials, J. Phys.: Condens. Matter **21**, 395502 (2009).

[41] P. Giannozzi, O. Andreussi, T. Brumme, O. Bunau, M. Buongiorno Nardelli, M. Calandra, R. Car, C. Cavazzoni, D. Ceresoli, M. Cococcioni *et al.*, Advanced capabilities for materials modelling with QUANTUM ESPRESSO, J. Phys.: Condens. Matter **29**, 465901 (2017).

[42] J.-M. Lihm, M. Ghim, S.-J. Hong, and C.-H. Park, Accurate calculation of Wannier centers, spreads, and position-related matrix elements (unpublished).

[43] See Supplemental Material at http://link.aps.org/supplemental/10.1103/56cw-5h19 for a detailed workflow of the implementation and additional relevant computational details and tests.

[44] J. P. Perdew and A. Zunger, Self-interaction correction to density-functional approximations for many-electron systems, Phys. Rev. B **23**, 5048 (1981).

[45] J. P. Perdew, K. Burke, and M. Ernzerhof, Generalized gradient approximation made simple, Phys. Rev. Lett. **77**, 3865 (1996).

[46] J. Heyd, G. E. Scuseria, and M. Ernzerhof, Hybrid functionals based on a screened Coulomb potential, J. Chem. Phys. **118**, 8207 (2003).

[47] D. R. Hamann, Optimized norm-conserving Vanderbilt pseudopotentials, Phys. Rev. B **88**, 085117 (2013).

[48] H. J. Monkhorst and J. D. Pack, Special points for Brillouin-zone integrations, Phys. Rev. B **13**, 5188 (1976).

[49] A. Damle, L. Lin, and L. Ying, Compressed representation of Kohn–Sham orbitals via selected columns of the density matrix, J. Chem. Theory Comput. **11**, 1463 (2015).

[50] A. Damle and L. Lin, Disentanglement via entanglement: A unified method for Wannier localization, Multiscale Model. Simul. **16**, 1392 (2018).

[51] V. Vitale, G. Pizzi, A. Marrazzo, J. R. Yates, N. Marzari, and A. A. Mostofi, Automated high-throughput wannierisation, npj Comput. Mater. **6**, 66 (2020).

[52] V. B. Anzin, M. I. Eremets, Y. V. Kosichkin, A. I. Nadezhdinskii, and A. M. Shirokov, Measurement of the energy gap in tellurium under pressure, Phys. Status Solidi A **42**, 385 (1977).

[53] In Ref. [22], the quantity $\bar{\rho}(0)$ was calculated for right-handed crystals. To compare with our results for left-handed crystals, in Table II we flip the sign of the $\bar{\rho}(0)$ values reported in that work.

[54] E. Assmann, P. Wissgott, J. Kuneš, A. Toschi, P. Blaha, and K. Held, Woptic: Optical conductivity with Wannier functions and adaptive k-mesh refinement, Comput. Phys. Commun. **202**, 1 (2016).

[55] J.-P. Hanke, F. Freimuth, A. K. Nandy, H. Zhang, S. Blügel, and Y. Mokrousov, Role of Berry phase theory for describing orbital magnetism: From magnetic heterostructures to topological orbital ferromagnets, Phys. Rev. B **94**, 121114(R) (2016).

[56] A. Marrazzo, S. Beck, E. R. Margine, N. Marzari, A. A. Mostofi, J. Qiao, I. Souza, S. S. Tsirkin, J. R. Yates, and G. Pizzi, Wannier-function software ecosystem for materials simulations, Rev. Mod. Phys. **96**, 045008 (2024).

[57] A. Urru, I. Souza, S. S. Tsirkin, O. Pozo Ocaña, and D. Vanderbilt, Data relative to manuscript "Optical spatial dispersion via Wannier interpolation (2025)" [Data set], Zenodo, https://zenodo.org/records/15236403.

[58] D. B. Melrose and R. C. McPhedran, *Electromagnetic Processes in Dispersive Media* (Cambridge University Press, Cambridge, 1991).

[59] The tensor $B_{\alpha\beta}$ in Ref. [21] is equal to $\mathcal{T}_{\alpha\beta}$ in Eq. (17) without the $v_\alpha A_\beta$ term in Eq. (18) for $\mathcal{K}_{\alpha\beta}$. That accidental omission explains the missing terms in the expressions for $\mathfrak{m}_{\alpha\beta}$ and $\mathfrak{q}_{\alpha\beta}$ in Ref. [21]: see Eqs. (A13)–(A16) below and related discussion. Nevertheless, those terms were correctly included, although classified as E1 ("band dispersive") contributions, in the expression for $\sigma_{\alpha\beta\gamma}(\omega)$ given in that work, which is consistent with Eq. (13).

[60] To compare Eq. (A16) with Eq. (24c) of Ref. [21], multiply the latter by ω_{ln} and then use $\omega_{ln}/(\omega_{lp}\omega_{pn}) = 1/\omega_{lp} + 1/\omega_{pn}$.

[61] A. Pezo, D. García Ovalle, and A. Manchon, Orbital Hall effect in crystals: Interatomic versus intra-atomic contributions, Phys. Rev. B **106**, 104414 (2022).

[62] B. Göbel and I. Mertig, Orbital Hall effect accompanying quantum Hall effect: Landau levels cause orbital polarized edge currents, Phys. Rev. Lett. **133**, 146301 (2024).

[63] Y. Gao and D. Xiao, Nonreciprocal directional dichroism induced by the quantum metric dipole, Phys. Rev. Lett. **122**, 227402 (2019).

[64] D. Xiao, J. Shi, and Q. Niu, Berry phase correction to electron density of states in solids, Phys. Rev. Lett. **95**, 137204 (2005).

[65] M. Stengel and N. A. Spaldin, Accurate polarization within a unified Wannier function formalism, Phys. Rev. B **73**, 075121 (2006).

[66] D. Gresch, Q. Wu, G. W. Winkler, R. Häuselmann, M. Troyer, and A. A. Soluyanov, Automated construction of symmetrized Wannier-like tight-binding models from *ab initio* calculations, Phys. Rev. Mater. **2**, 103805 (2018).

[67] X. Liu, Simulation of nonlinear electronic transport using Wannier interpolation, Ph.D. thesis, University of Zürich, 2023.

[68] R. Sakuma, Symmetry-adapted Wannier functions in the maximal localization procedure, Phys. Rev. B **87**, 235109 (2013).

[69] Recently, the construction of symmetry-adapted Wannier functions with frozen energy windows and with SOC was implemented in WannierBerri. However, the present work did not make use of this development.